UNIVERSITY OF OKLAHOMA

GRADUATE COLLEGE

TORTUOSITY OF TIGHT ROCKS

A THESIS

SUBMITTED TO THE GRADUATE FACULTY

in partial fulfillment of the requirements for the

Degree of

MASTER OF SCIENCE

By

JUDAH ODIACHI
Norman, Oklahoma
2022

TORTUOSITY OF TIGHT ROCKS

A THESIS APPROVED FOR THE
MEWBOURNE SCHOOL OF PETROLEUM AND GEOLOGICAL ENGINEERING

BY THE COMMITTEE CONSISTING OF

Dr. Ali Tinni, Chair

Dr. Chandra S. Rai

Dr. Deepak Devegowda

© Copyright by JUDAH ODIACHI 2022
All Rights Reserved.

Dedicated to

God

Acknowledgements

I would like to thank my advisor, Dr. Ali Tinni for giving me this opportunity to pursue research under his guidance. His support and motivation have helped me grow professionally and personally. I am thankful to Dr. Chandra Rai and Dr. Deepak Devegowda for their valuable inputs towards my research and academics.

I would also like to thank Dr. Son Dang, for his mentorship and for helping me become a better researcher. I am thankful to Dr. Curtis, Mikki, Gary and my friends at IC^3 for their support, friendship and care.

Finally, I would like to express gratitude to my parents: Mr and Mrs Odiachi, and sisters: Sarah, Anna and Hephzibah for believing in me and for their unconditional love. Special shoutout to my extended family in the United States; the Ojuolape's for their support and encouragement, and friends met at OU: Oyindamola Obisesan, Michael Olubode, Joy Foluso, and members of the Nigerian OU community. My OU journey would not have been fun without you guys.

Table of Contents

List of Figures

List of Tables

Abstract

Tortuosity is a rock property that controls transport processes in porous media. It is essential in advective, diffusive transport and flow of electric current, especially in tight rocks which are characterized by low porosity and low permeability such as unconventional shale reservoirs. However, experimental values of diffusional and electrical tortuosity of tight rocks are scarce in the literature. To improve the understanding of diffusive transport and electrical flow in unconventional tight rock reservoirs, I have measured and compared the diffusional and electrical tortuosities of 12 tight rock samples from Utica, Bakken, Wolfcamp, and Eagle Ford formations and 3 sandstones from Berea, Lyon and Illinois Basin.

For this study, the samples selected were characterized by measurements of total organic carbon (TOC), mineralogy, porosity, and pore size distributions using scanning electron microscopy image analysis, mercury injection capillary pressure, and subcritical nitrogen adsorption. Upon characterization, the samples were soxhlet-extracted with methanol and dried at 100°C before saturating with 25,000 ppm KCl brine. To measure diffusional tortuosity, the brine saturated samples were immersed into D_2O to allow the diffusion of D_2O into the samples. The rates at which D_2O diffused into the samples were measured with 12 MHz NMR instruments. The effective pore fluid diffusion coefficient of D_2O and the bulk diffusion coefficient of D_2O were used to compute the diffusional tortuosities.

To measure the electrical tortuosities, the samples were resaturated with 25,000 ppm KCl brine before immersion into 60,000 ppm KCl brine. The measurements of the samples' resistivities as a function of time after the immersion into the 60,000 ppm KCl brine were used to compute effective pore ionic diffusion coefficients. These effective pore ionic diffusion coefficients were used in

combination with the ionic bulk diffusion coefficient to compute the electrical tortuosity of the samples.

Our measurements show that the diffusional tortuosity and electrical tortuosity have similar values. Therefore fluid diffusion and electrical conduction are controlled by the same flow path.

These tortuosities in the tight rock samples range between 1.8 to 5.8, while the sandstones range between 1.4 to 3.9.

A method to determine effective porosity was also developed and it was observed that the effective porosity in the tight rocks ranged between 45 - 93% of the total porosity, while the sandstones had effective porosities approximately equal to the total porosity.

For the unconventional tight rock samples studied, it is observed that TOC exerts a primary control on the diffusional and electrical tortuosity as well as effective porosity of tight rocks.

The observations made in this study indicate that electrical and diffusive flow are controlled by the same flow path. Therefore, electrical tortuosity from resistivity formation factor measurements can be used in place of diffusional tortuosities in huff-n-puff EOR design and optimization because the electrical tortuosity measurements can be performed in minutes while diffusional tortuosity measurements take weeks to complete. Also, the knowledge of electrical tortuosity is important in determining electrical parameters to accurately determine the water saturation.

Chapter 1 : Introduction

Oil production from unconventional reservoirs has increased from 12% in 2008 to 60% of the total United States oil production in 2019 (EIA, 2019) (**Figure 1-1**).

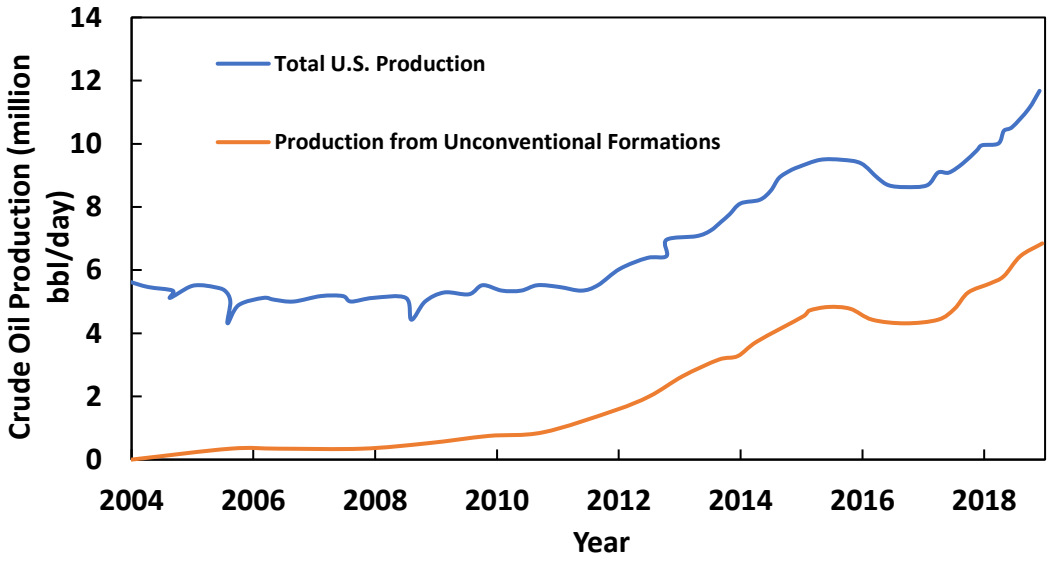

Figure 1-1. Total U.S. crude oil production and crude oil production from unconventional formations from 2004 to 2019. Crude oil production from unconventional reservoirs started in the 1990s before rapidly increasing in 2010 (EIA, 2019).

Despite the improvements in oil production from unconventional reservoirs, the exploitation of these reservoirs remains challenging, as demonstrated by their oil recovery factors lower than 7% (US DOE, 2013; Sheng, 2015; Todd & Evans, 2016; Cronin et al., 2019).

Tabibi & Emadi (2003); Fleury et al. (2004) have reported some of the complexity associated with estimating fundamental parameters such as water saturation from resistivity logs in unconventional reservoirs. Also, successful predictions of fluid flow properties such as permeability from basic reservoir rock properties of tight rocks e.g. shales are limited (Duda et al., 2011; Srisutthiyakorn & Mavko, 2016; Bauer et al., 2017).

To improve the low oil recovery factors observed during the primary depletion of unconventional tight rocks, operators have used enhanced oil recovery (EOR) techniques such as huff-n-puff gas injection. However, the optimization of huff-n-puff EOR in unconventional formations is often achieved via a costly trial and error process (Nguyen et al., 2015; Hoffman & Rutledge, 2019; Dang et al., 2021).

The challenges aforementioned are partly due to the gaps in the current understanding of how the microstructure of tight rock reservoirs controls the response of resistivity tools (Bustin et al., 2008; Labani & Rezaee, 2015; Kadkhodaie & Rezaee, 2016) and fluid flow (Salama et al., 2017; Garum et al., 2019; Odiachi et al., 2021).

Tortuosity is a parameter often used to describe flow pathways in porous media. It is generally used as a measure of how the interconnectedness and sinuosity of the pore space affect transport properties. Researchers have defined tortuosity in relation to geometric, hydraulic, diffusion, or electric properties of porous media (Dullien, 1992; Clennell, 1997; Ghanbarian et al., 2013).

Due to the complexities associated with true tortuosity measurements, tortuosity has also been used as a fitting parameter between model predictions and experimental observations (Fatt, 1956; Dullien, 1992). However, several authors have successfully measured the geometrical, hydraulic, diffusional and electrical tortuosity of conventional rocks (Winsauer et al., 1952; Chen et al., 1977; Garrouch et al., 2001; Srisutthiyakorn & Mavko, 2016; Gong et al., 2020; Leger & Luquot, 2021). Researchers have also examined the relationships between these tortuosities with the major disagreements centering around whether or not the diffusional and electrical tortuosity are similar and thus comparable (Klinkenberg, 1951; Garrouch et al., 2001; Bezzar & Ghomari, 2013).

Also, a limited number of tortuosity measurements for tight rocks are available in literature (Dang et al., 2018, 2021; Almasoodi & Reza, 2019). However, the published values of diffusional and

electrical tortuosity do not allow a proper investigation of the petrophysical factors that could control them and the establishment of predictive models for tortuosity.

In addition to tortuosity, effective porosity plays an important role in the transport of matter through porous media. It is a parameter required for most transport models (Marsily, 1986; Fetter, 1988, 1993; Zheng & Bennett, 2002). However, there are no adequate laboratory protocols for effective porosity measurements in tight rocks.

1.2 Scope of the Thesis

The present thesis is a summary of an experimental program designed to improve the current understanding of diffusional and electrical tortuosity in unconventional tight rocks. Measurements of electrical and diffusional tortuosities were conducted on 12 tight rock samples collected from Utica, Bakken, Eagle Ford, and Wolfcamp formations and 3 sandstone samples from the Berea formation, Lyon formation, and Illinois Basin. Also, a method to determine effective porosity using the tortuosity measurements in these samples was developed. The rock samples used during this thesis were extensively characterized prior to the measurements of tortuosities and effective porosity. The large dataset of electrical tortuosity, diffusional tortuosity, and effective porosity constituted during this thesis was used to:

- Compare the independent measurements of the diffusional and electrical tortuosity.
- Investigate the petrophysical parameters controlling tortuosity.
- Investigate the petrophysical parameters controlling effective porosity.

1.3 Organization of the Thesis

This thesis is divided into five chapters and is presented as follows:

- Chapter 1 introduces the motivation and describes the scope of this study.
- Chapter 2 presents a literature review on shales microstructure, effective porosity, and tortuosity in porous media.
- Chapter 3 details the equipment and experimental methods for tortuosity, effective porosity experiments, and petrophysical rock properties.
- Chapter 4 presents the measurements of diffusional tortuosity, electrical tortuosity, effective porosity, and comparisons between the tortuosity measures.
- Chapter 5 details the petrophysical parameters controlling tortuosity and effective porosity.
- Chapter 6 presents the conclusion and the most significant findings.

Chapter 2 : Literature Review

2.1 Microstructure of Shales

Unconventional shale reservoirs are fine grain multimineral rocks that contain solid organic matter. The heterogeneity in their composition is mainly responsible for their complex microstructure, which controls reservoir properties that govern transport such as pore structure, porosity, and permeability (**Figure 2-1**).

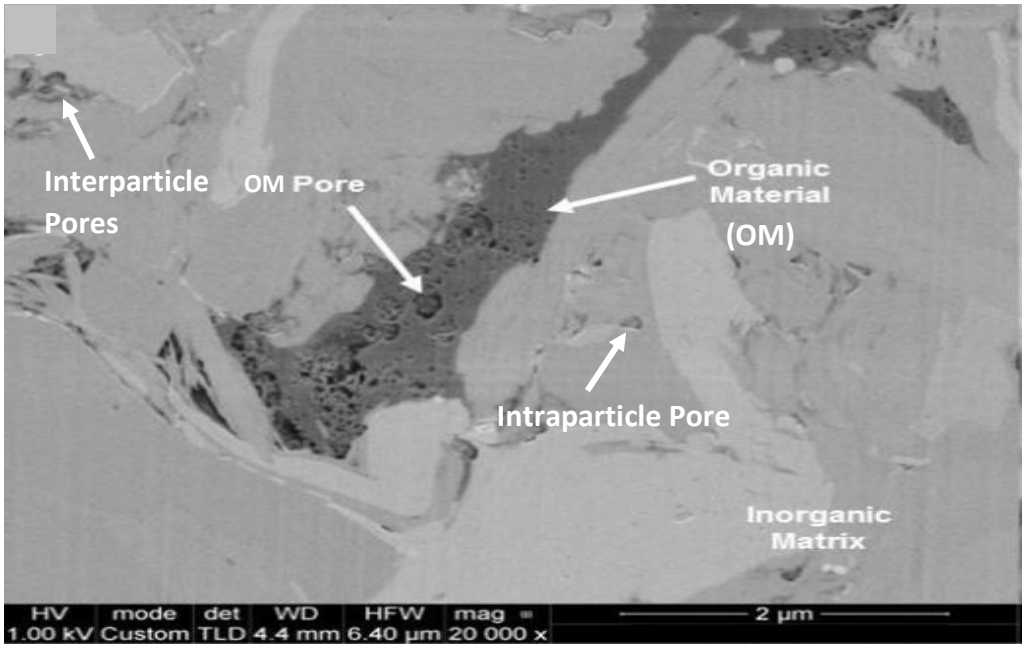

Figure 2-1. SEM image of the pore types in a shale sample from the Marcellus formation (Curtis et al., 2011a) showing the presence of interparticle pores, intraparticle pores, and organic matter pores.

Shale reservoirs have pores between the inorganic particles (inorganic porosity), within the organic matter (intraparticle porosity), and between the organic and inorganic minerals (interparticle porosity) (**Figure 2-1**) (Curtis et al., 2011a; Loucks et al., 2011).

Nelson (2009) and Zou et al. (2015) have shown that the pore throats of shale reservoirs have peak diameter ranging between 8 and 50 nm, while Bustin et al. (2008); Curtis et al. (2012); Kuila & Prasad (2013); Er et al. (2016) have reported pore body diameter peaks between 100 and 2000 nm.

To study the connectivity between the pores of unconventional shale reservoirs Hu et al. (2014); Klaver et al. (2015); Zhao et al. (2020) have used MICP measurements and wood's metal injection into shales in combination with Scanning Electron Microscopy (SEM). Klaver et al. (2015) observed that liquid metal injection into the pores provided high resolution details regarding pore structure and connectivity. Klaver et al. (2015) have also shown that during MICP measurements, compressibility could close small pore throats.

Tinni (2015) found that shales have water and oil wet pores which could be arranged either in series or parallel which gives rise to the development of different pore connectivity models.

Unlike conventional formations, pore connectivity in shales is usually low, thus the flow paths are highly tortuous (Hu et al., 2012; Backeberg et al., 2017; Qinhong et al., 2017); hence knowledge of tortuosity is important to understanding fluid transport.

2.2 Effective Porosity

Effective porosity is the interconnected pore volume that contributes to transport in porous media. However, some researchers have defined it as the porosity resulting from the difference between the total porosity and the clay bound water (Worthington, 1998; Ezekwe, 2010; Spooner, 2014) while Eslinger & Pevear (1985); Peveraro & Thomas (2010); McPhee et al. (2015) defined effective porosity as the porosity resulting from the difference between total porosity and the clay volume. This definition makes a drastic assumption that clays have no effective porosity which has been proven to be inaccurate (Loucks et al., 2011; Curtis et al., 2012; Spooner, 2014).

Imbibition, tracer concentration profiles, and imaging methods are experimental methods that have been used to determine effective porosity (Hu et al., 2012; Ma et al., 2020). Using SEM images,

Curtis et al. (2011b) noted that the effective porosity in a Marcellus shale sample was about 19% of the total porosity.

From the analysis of MICP data Davudov et al. (2018) noted that the effective porosity was about 30% of the total porosity for samples from the Barnett and Haynesville formation. Davudov et al. (2018) also observed a strong positive linear relationship between effective porosity and total porosity for shale samples from the Barnett formation.

Due to the low total porosity values usually encountered in shales, it is important to have a good understanding of the effective porosity to model and predict flow properties which could help reduce the challenges encountered in optimal exploitation of these shale reservoirs.

2.3 Tortuosity in Porous Media

2.3.1 Geometrical Tortuosity

In an idealized medium where the pore system can be represented by a single capillary (**Figure 2-2**), the geometrical tortuosity (τ_g) is the ratio of pore length (Le) over the length of the sample (L).

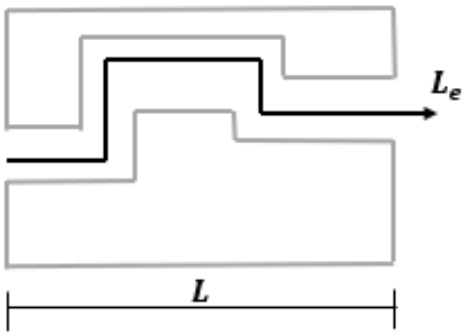

Figure 2-2. Schematic of a porous medium of length (L) with a pore structure that can be represented by a capillary tube with pore length (Le)

However, porous media are generally complex assemblies of grains (**Figure 2-3**). Therefore, geometrical tortuosity is better defined as the ratio of the shortest continuous tortuous path (l_{min}) to the straight-line length (l).

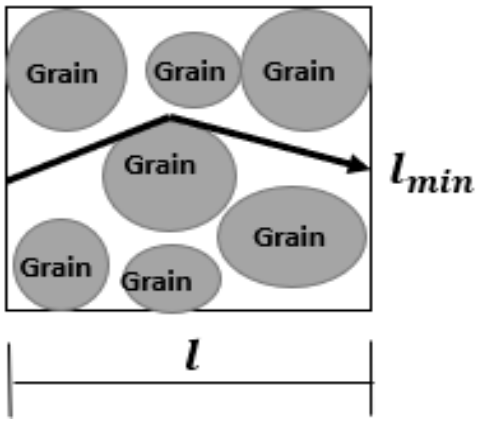

Figure 2-3. Schematic of porous medium constituted by solid grains. l_{min} represents the shortest continuous tortuous path, and l represents the straight line length of the flow direction.

$$\tau_g = \frac{l_{min(a,b)}}{l} \tag{2.1}$$

Geometrical tortuosity is a fundamental rock property because it does not depend on transport properties. To predict geometrical tortuosity, researchers have modeled porous media as two-dimensional porous media consisting of square solid particles (Bo-Ming & Jian-Hua, 2004) , fixed bed of randomly packed spherical particles (Lanfrey et al., 2010) and fractal pore models (Li & Yu, 2011). As shown by **Figure 2-4**, these different models depend on the rock's porosity.

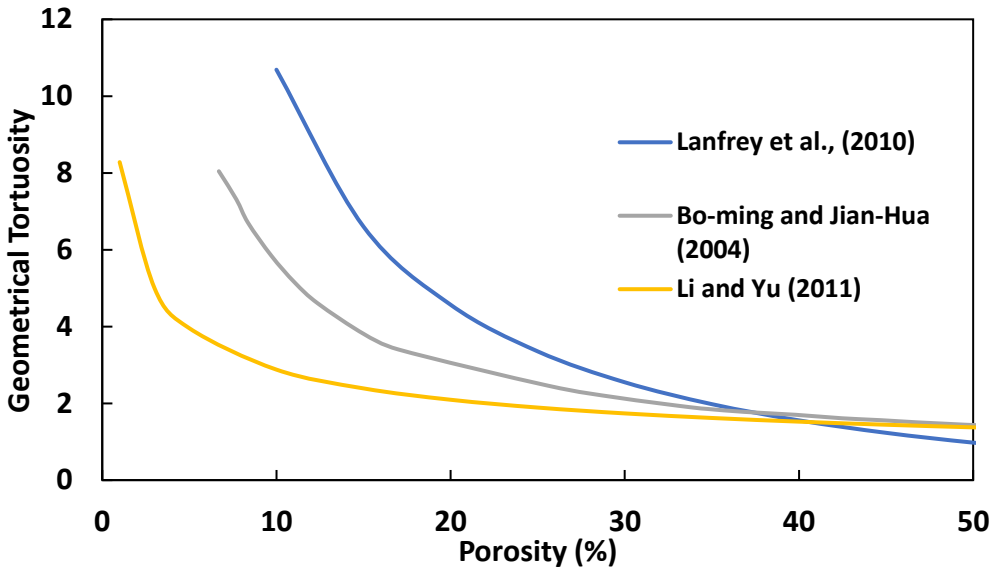

Figure 2-4. Geometrical tortuosity prediction using the models of Bo-ming and Jian-Hua (2004), Lanfrey et al., (2010), and Li and Yu (2011). Below 30% porosity, it is observed that Lanfrey et al., (2020) model shows the highest values while Li and Yu (2011) shows the lowest values. But at 40% porosity, a convergence of values in Bo-ming and Jian-Hua (2004) and Li and Yu (2011) models is observed.

Measurements of τ_g generally rely on the estimation of the tortuous length from pore structure images obtained from optical microscopy (Georgali & Tsakiridis, 2005), X-ray micro-computed tomography (Spanne et al., 1994; Amien et al., 2019), scanning electron microscopy (Stutzman, 2004; Munroe, 2009; Gong et al., 2020; Leite Roque & Nardelli Siebert, 2020; Fu et al., 2021).

Gong et al., (2020); Leite Roque & Nardelli Siebert (2020); Fu et al., (2021) reported τ_g values between 1.0 and 4.0 for sandstones while Roque and Siebert, (2020) showed that τ_g varies between 1.4 and 1.9 for carbonates. In shales, τ_g values between 5.0 and 10.0 have been reported (Qinhong et al., 2017; Zhang et al., 2019). **Figure 2-5** presents the experimental values of τ_g measured by researchers aforementioned along with the predictions of models developed by Bo-Ming & Jian-Hua (2004); Lanfrey et al. (2010); Li & Yu (2011). I observed that the data of Gong et al., (2020) on sandstone samples obey the model of Li & Yu (2011). Similar to the trends

from the analytical model, the experimental data show a negative relationship between τ_g and porosity.

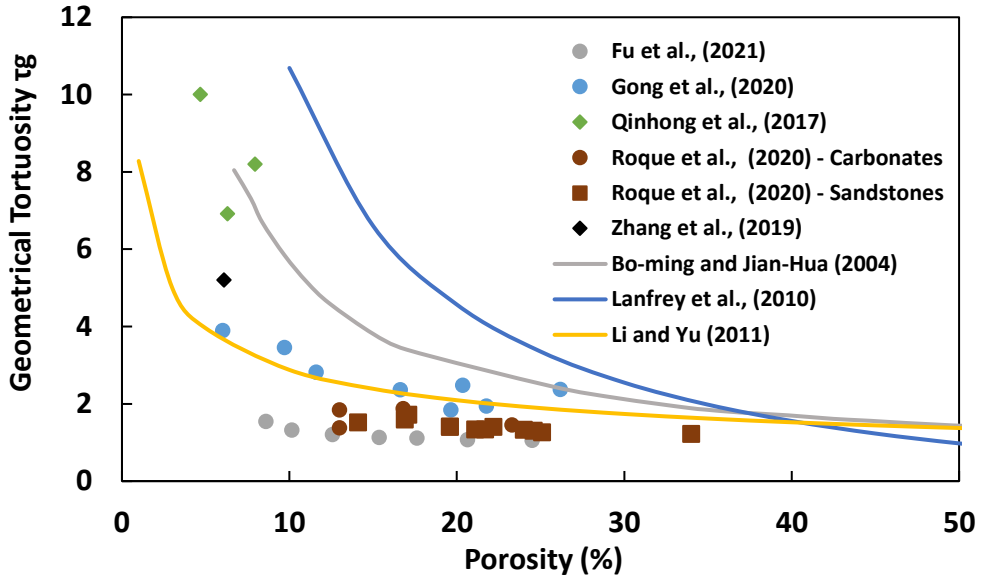

Figure 2-5. Measured values of geometrical tortuosity and models predictions. The experimental measurements are represented by symbols, while the models are represented by solid lines. It is observed that the experimental values of Gong et al., (2020) agree with model results from Li and Yu (2021).

2.3.2 Hydraulic Tortuosity

During laminar flow in porous media, the streamlines are affected by the grain shapes and the pore constrictions (**Figure 2-6**) whereas the geometrical tortuosity is primarily dependent on the shortest continuous tortuous path and does not depend on transport properties. Therefore, it is expected that hydraulic tortuosity will be different from geometrical tortuosity.

Hydraulic tortuosity is defined as the ratio of the average flow path length, i.e., effective path length (l_{eh}) to the straight-line length in the direction of flow (l) (Eq. 2.2) (Kozeny, 1927; Carman, 1937; Srisutthiyakorn & Mavko, 2016; Garcia et al., 2018).

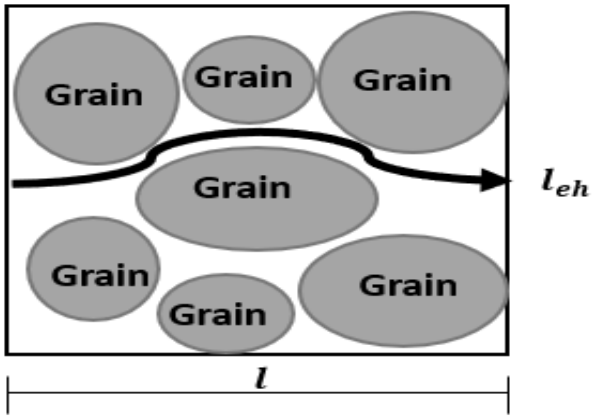

Figure 2-6. Schematic representation of the hydraulic tortuosity as the ratio of the effective path length of the fluid through streamlines (l_{eh}) to the straight line length in the direction of flow.

$$\tau_h = \frac{l_{eh}}{l} \tag{2.2}$$

Hydraulic tortuosity has been analytically modeled by Du Plessis & Masliyah (1991) and Ahmadi et al. (2011) using volumetric averaging approaches in isotropic granular media and monosized spheres respectively. As shown by **Figure 2-7**, these different models depend on porosity.

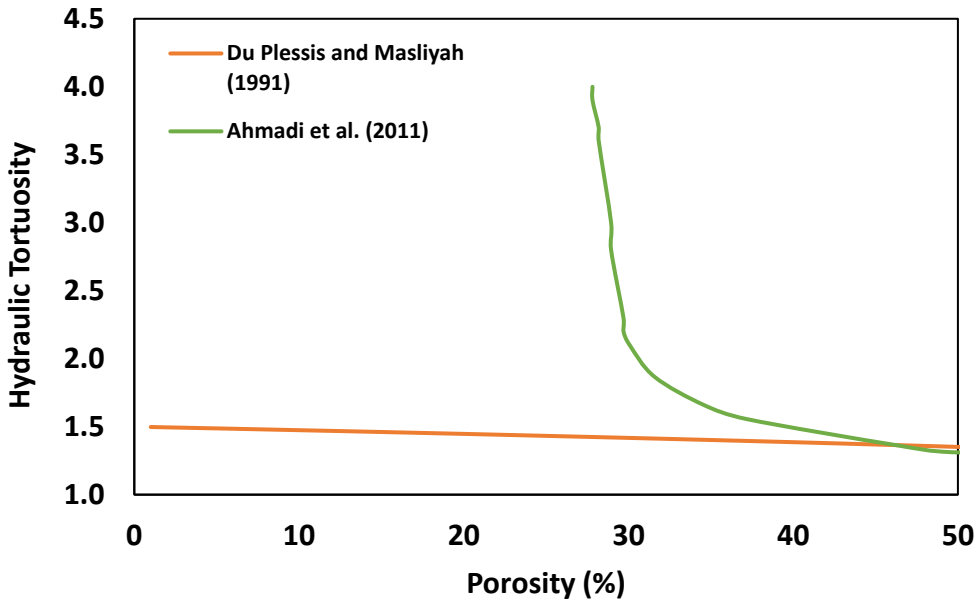

Figure 2-7. Hydraulic tortuosity predictions using the models of Du Plessis and Masliyah (1991) and Ahmadi et al., (2011). Below 40% porosity, it is observed that Ahmadi et al. (2011) model predicts higher hydraulic tortuosity values while above 45% porosity, a convergence of model values is observed.

Numerical methods such as Lattice Boltzmann simulations (LBM) and Finite Volume Method (FVM) on 3-D binary segmented images have been used to directly calculate hydraulic tortuosity by analyzing streamlines obtained from the simulations (Fredrich et al., 1999; Keehm, 2003; Jin et al., 2004; Piller et al., 2009; Srisutthiyakorn & Mavko, 2016; Roque & Siebert, 2020; Leger & Luquot, 2021).

To understand the impact of hydraulic tortuosity on permeability, consider an idealized medium, such as represented in **Figure 2-2** above.

The velocity in the pore of such a system can be obtained from Poiseuille's equation Eq. (2.3)

$$v_p = \frac{\pi r^4 \Delta p}{8 A_p \mu L_e} \tag{2.3}$$

where v_p is the flow velocity in the pore (m/s), Δp is the pressure differential between the ends of the tube (N/m^2), r is the capillary radius (m), A_p is the pore cross-sectional-area (m^2), L_e is the effective length of the pore (m), and μ is the viscosity of the fluid (Ns/m^2).

The flow velocity, v can also be computed by the product of the intrinsic phase average velocity (pore velocity) v_p and porosity, Ø (Epstein, 1989; Clennell, 1997). However, in a porous medium characterized by tortuous paths where the path length for fluid flow is longer than the length of the porous medium, the pore velocity is:

$$v_p = \frac{v}{Ø} * \frac{L_e}{L} \tag{2.4}$$

Substituting equation (2.4) into equation (2.3), to obtain Eq. (2.5)

$$\Delta P = \frac{8A_p \mu v L}{Ø \pi r^4} * \left(\frac{\mathrm{L_e}}{L}\right)^2 \tag{2.5}$$

Recalling Eq. (2.2), Eq. (2.5) becomes

$$\Delta P = \frac{8A_p \mu v L}{Ø \pi r^4} * \tau^2 \tag{2.6}$$

Therefore, Darcy's law for one-dimensional flow becomes,

$$\mathrm{K} = \frac{Ø \pi r^4}{8A_p \tau^2} \tag{2.7}$$

Eq. (2.7) shows that permeability is inversely proportional to the square of hydraulic tortuosity. In practice, researchers have used equations similar to Eq. (2.7) to determine the hydraulic tortuosity of porous media after permeability measurements and knowing the pore throat radius.

Figure 2-8 presents the negative relationship observed between hydraulic tortuosity and porosity in sandstones ranging between 1.2 and 1.6 and carbonates between 1.2 and 1.8, as reported by Srisutthiyakorn & Mavko (2016), while Leger & Luquot (2021) reported hydraulic tortuosity for chalk, entrochal limestone and dolomite carbonates ranging between 1.6 and 1.8, 2.5 and 3.0, and 1.5 and 3.0 respectively, and Roque et al. (2020) reported values between 1.5 and 2.0. There are limited reported values in the literature for shale formations, but Almasoodi & Reza (2019) reported a hydraulic tortuosity value of 1.4 in a shale sample.

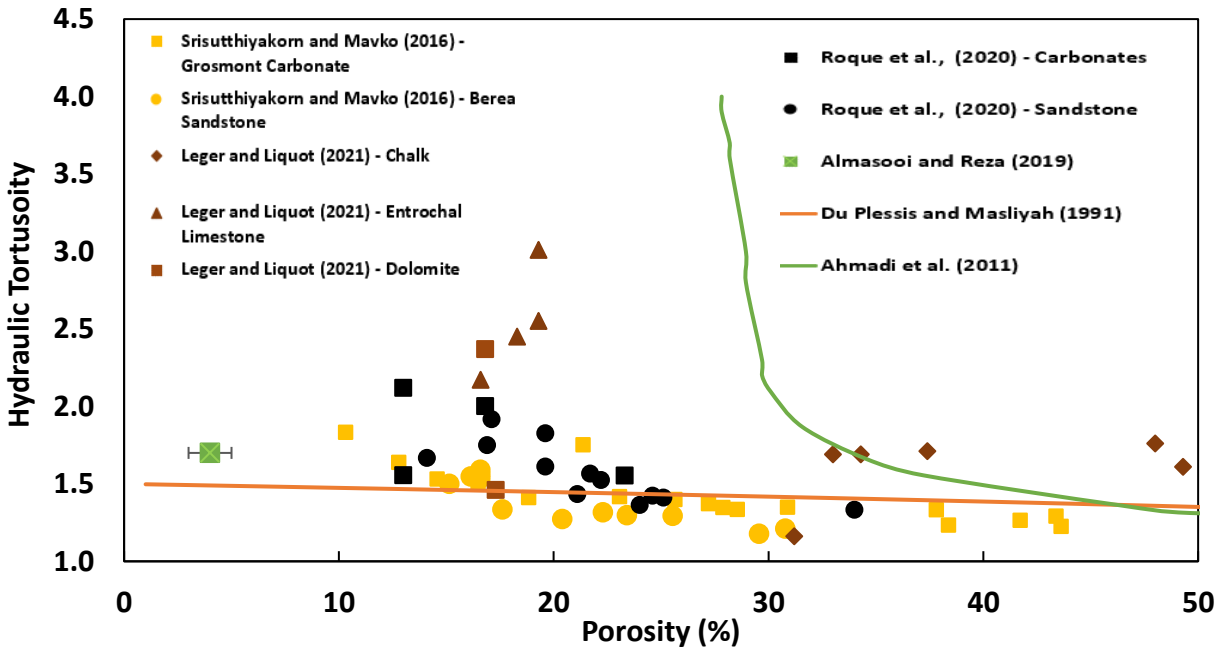

Figure 2-8. Measured values of hydraulic tortuosity and models predictions. The experimental measurements are represented by symbols, while the models are represented by solid lines. The experimental values by Srisutthiyakorn & Mavko (2016) agree with model results from Du Plessis and Masliyah (1991) for the sandstone and carbonate samples.

Part of the difference between the hydraulic and geometrical tortuosity can be attributed to the fact that the fluid flow path in the porous medium are streamlines (**Figure 2-5**) rather than being tangential to the rock grains as depicted by the geometrical tortuosity (**Figure 2-2**). Also, fluid

flow is retarded at the channel walls than the channel axes due to viscous drag, hence the preference for certain flow paths (Coussy, 1995; Clennell, 1997).

Features of the pore geometry such as constriction effects related to changes in pore throat diameter also reduce flow efficiency (**Figure 2-9**), implying an increased tortuosity (Azzam & Dullien, 1977; Bernabe, 1991; Dullien, 1992; Clennell, 1997).

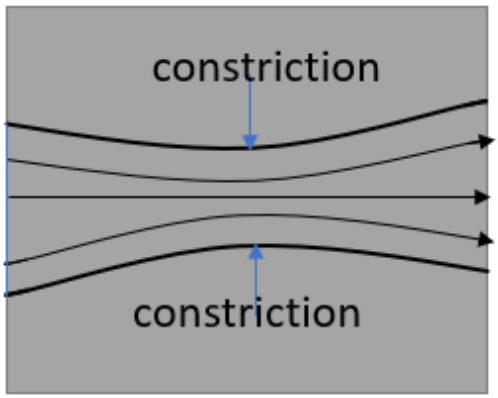

Figure 2-9. Schematic showing change in pore throat diameter due to constriction effects. The flow lines (black arrowheads) conform to the change in the flow path reducing flow efficiency.

2.3.3 Diffusional Tortuosity

Diffusion is a random motion of molecules driven by a concentration gradient. Diffusional tortuosity is defined as the ratio of the square root of the diffusing species in free fluid, D_b to the effective diffusion coefficient, D_e in porous media (Eq. 2.8) (Petersen, 1958; van Brakel & Heertjes, 1974; Ullman & Aller, 1982; Epstein, 1989). The effective diffusion coefficient is dependent on retardation effects such as bulges and constrictions imposed by the porous media on diffusion.

$$\tau_d = \sqrt{\frac{D_b}{D_e}} \tag{2.8}$$

Diffusional tortuosity in porous media has been modeled analytically by Weissberg (1963) in a randomly overlapping bed of spherical particles and Beeckman (1990) in a heterogeneous catalyst. These models predict that diffusional tortuosity will increase when there is a decrease in porosity (**Figure 2-10**).

To measure the diffusional tortuosity of porous media, the bulk diffusional coefficients can be determined using methods such as PVT cell (Riazi, 1996), using nuclear magnetic resonance (NMR) 1-D gradient measurements (Jamialahmadi et al., 2006), infra-red spectroscopy measurements (Dang et al., 2018), oil swelling measurements (Mukherjee et al., 2020). Effective diffusion coefficients can be measured using pressure decay measurements (Chen et al., 2018; Shi et al., 2018; Janiga et al., 2020; Z. Li et al., 2021), NMR diffusion measurements (Dang et al., 2021; Fleury et al., 2020).

Chen et al. (1977), Dang et al. (2018, 2021) and Fleury et al. (2009, 2010, 2016) reported diffusional tortuosity values as the ratio of the bulk diffusion coefficient to the effective diffusion coefficient in porous media. However, to be consistent with the true definition of diffusional tortuosity in Eq. (2.8), I recomputed the diffusional tortuosities as the squared root of the diffusional tortuosities published by Chen et al. (1977), Dang et al. (2018, 2021) and Fleury et al. (2009, 2010, 2016).

The corrected values of diffusional tortuosity by Chen et al. (1977) ranged between 1 and 3.8 for sandstones with porosity ranging between 2 and 47%. The diffusional tortuosity values by Dang et al. (2018, 2021) ranged between 2 and 3.2 for Eagle Ford and Wolfcamp samples with porosity ranging between 3 and 10% porosity, while the values of Fleury et al. (2009, 2010, 2016) ranged between 1.8 and 6.5 for shale samples (**Figure 2-10**). As observed in the figure below, a negative

relationship between diffusional tortuosity and porosity is observed in the reported values by Weissberg (1963), Beeckman (1990) and Chen et al. (1977).

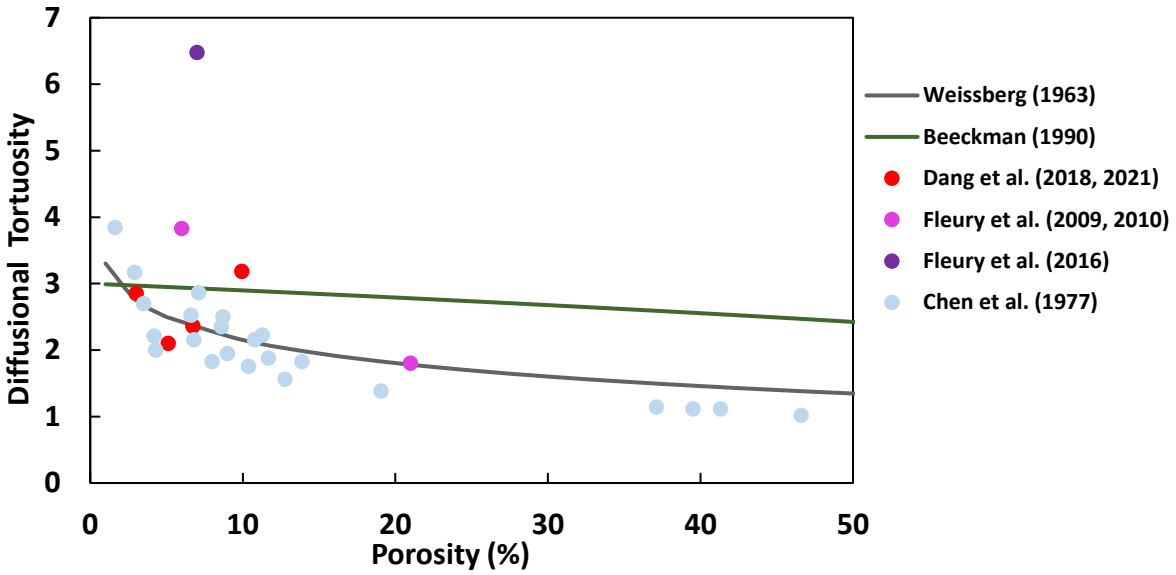

Figure 2-10. Measured values of diffusional tortuosity and models predictions. The experimental measurements are represented by symbols, while the models are represented by solid lines. At porosities larger than 10%, experimental values of sandstone samples, Fleury et al. (2009, 2010) and some of Dang et al. (2018, 2021) results agree with Weissberg (1963) analytical model.

2.3.4 Electrical Tortuosity

Electrical tortuosity can be defined as a ratio of the effective electrical length (L_{ee}) to straight-line length (L) in the direction of flow (Winsauer et al., 1952; Clennell, 1997; Cai et al., 2017).

$$\tau_e = \frac{L_{ee}}{L} \tag{2.9}$$

In porous media, electrical conductivity is due to the ions mobility in the brine contained in the pore spaces. However, minerals such as pyrite, magnetite, and hematite are also conductive and excess electrical conductivity has been observed in clay bearing rich rocks.

Maxwell (1873) and Coleman & Vassilicos (2008) modeled electrical tortuosity analytically in dilute suspension of non-conducting spheres and fractal media respectively and observed a negative dependence on porosity.

Winsauer et al. (1952) and Nguyen et al. (2015) have measured electrical tortuosity by measuring the effective diffusion of ions in a tortuous and porous medium. Knowing the effective pore ionic diffusion coefficient and bulk ionic diffusion coefficient, electrical tortuosity can be computed by Eq. (2.10).

$$\tau_e = \sqrt{\frac{D_{ionic\ bulk}}{D_{ionic\ eff}}} \tag{2.10}$$

Where τ_e is the electrical tortuosity, $D_{ionic\ bulk}$ is the bulk ionic diffusion coefficient and $D_{ionic\ eff}$ is the effective ionic diffusion coefficient of the ions in a porous medium. The effective ionic diffusion coefficient of the ions is dependent on retaradation effects such as bulges and constrictions that the porous medium has on electrical conduction which is governed by ion mobility.

However, the common expression of electrical tortuosity in the literature is Eq. (2.11) which is an expression of Archie's first law used for water saturation determination from electrical logs.

$$\tau_e = \sqrt{F\ * \emptyset_{eff}} \tag{2.11}$$

Where F is the resistivity formation factor and $\emptyset_{eff}$ represents the effective porosity. The resistivity formation factor is obtained from Archie's first law (Archie, 1942) Eq. (2.12).

$$F = \frac{R_o}{R_w} \tag{2.12}$$

Where R_o is the resistivity of the porous medium at 100% saturation and R_w is the brine resistivity. Winsauer et al. (1952) reported values for electrical tortuosity ranging between 1.6 and 3.3 for sandstones. Garrouch et al. (2001) reported values ranging between 1.7 and 2.3 for sandstone samples from Berea, Okesa, Tallant, and Elgin formations and Leger and Liquot (2021) reported values ranging between 1.7 and 5.3 for carbonate samples (**Figure 2-11**). A negative trend between

electrical tortuosity and porosity is observed in the experimental values (Winsauer et al. 1952; Garrouch et al. 2001; Leger and Liquot 2021) and analytical models (Maxwell, 1873 and Coleman & Vassilicos,2008) reported in the literature. Reported values of electrical tortuosity in shales are scarce in the literature, with Gonzalez et al. (2021) reporting values ranging between 1.0 and 1.5 for biogenic rock samples composed of sponge silica spicules.

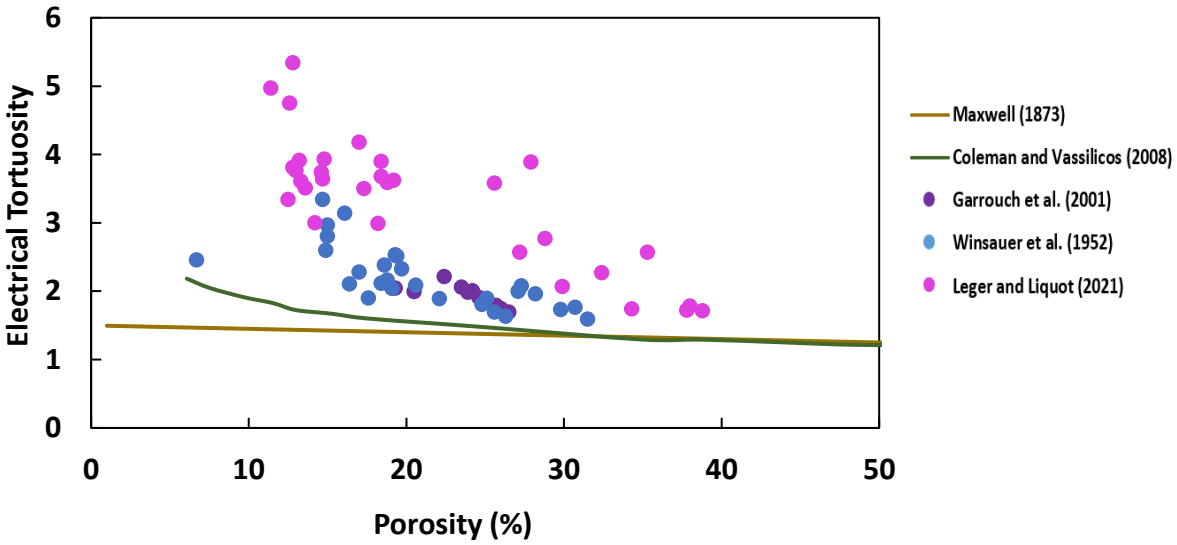

Figure 2-11. Measured values of electrical tortuosity and models predictions. The experimental measurements are represented by symbols, while the models are represented by solid lines. Below 30% porosity, the analytical models do not show similar values but at porosities larger than 30%, it is observed that Maxwell (1873) and Coleman and Vassillicos (2008) show similar values.

The difference between the electrical tortuosity and hydraulic tortuosity have been explained using numerical solutions of flow equations (Brown, 1989; Saomoto & Katagiri, 2015) and lattice gas automation methods (Zhang & Knackstedt, 1995) to track fluid flow paths and electrical flow. The results from the numerical solutions of the flow eqution indicate that hydraulic flow is more tortuous while showing a preference for certain channels than electrical flow (**Figure 2-12**).

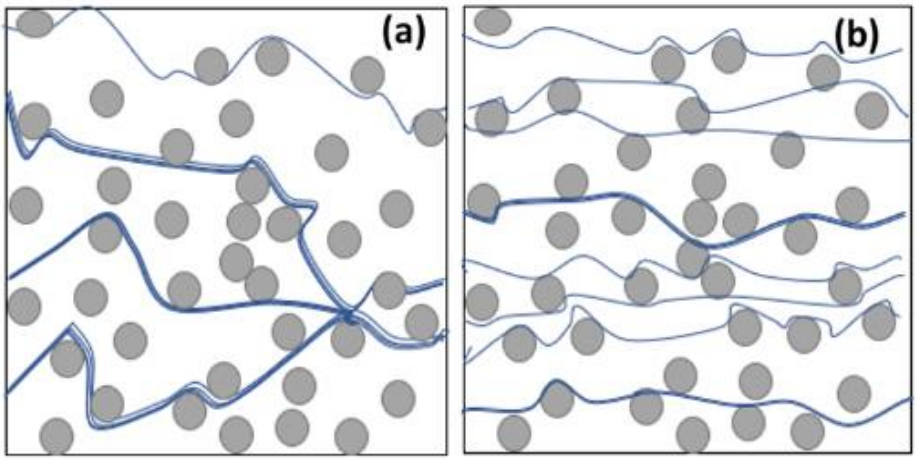

Figure 2-12. Schematic representation of hydraulic flow streamlines (a) and electric flow streamlines (b) in a circular particle packed porous medium of 70% porosity showing preferential flow paths for fluid flow, thus implying higher tortuosity in hydraulic flow Martys et al., (1994), Saomato & Katagiri (2015).

Saomoto & Katagiri (2015) showed that the hydraulic tortuosity is on average greater than the electrical tortuosity by 15% using finite element analysis simulations in circular and square particle packed porous media for a porosity range of 40 % - 90 % based on the Navier-Stokes equations of flow (**Figure 2-13**).

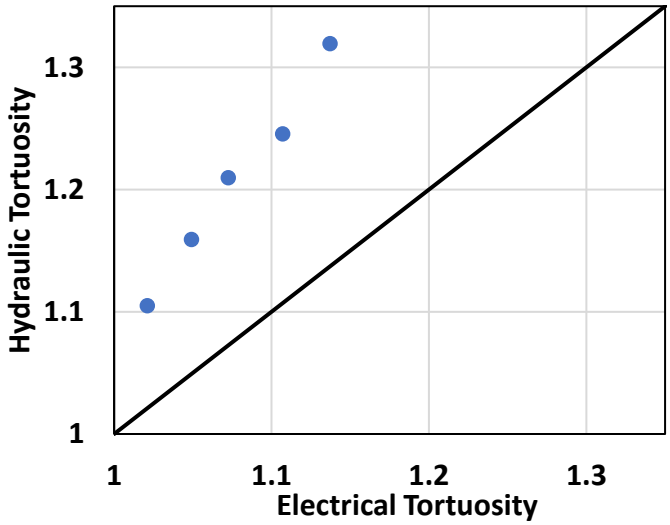

Figure 2-13. The relationship between hydraulic and electrical tortuosity shows that hydraulic tortuosity is a higher measure when compared with values of electrical tortuosity Saomoto & Katagiri, (2015).

Figure 2-14 illustrates the relationship between electrical and diffusional tortuosity from published values in literature. Klinkenberg (1951) results do not show agreement between the diffusional and electrical tortuosity. Garrouch et al. (2001) showed that the diffusional and electrical tortuosities on some sandstone samples of porosity range 19.3% - 26.5% were similar while Bezzar & Ghomari (2013) from measurements of sand-bentonite mixtures (90:10) claimed that both tortuosities were different due to significant differences observed in the actual effective diffusion coefficient obtained from diffusion experiments and the effective diffusion coefficient from electrical tortuosity measurements.

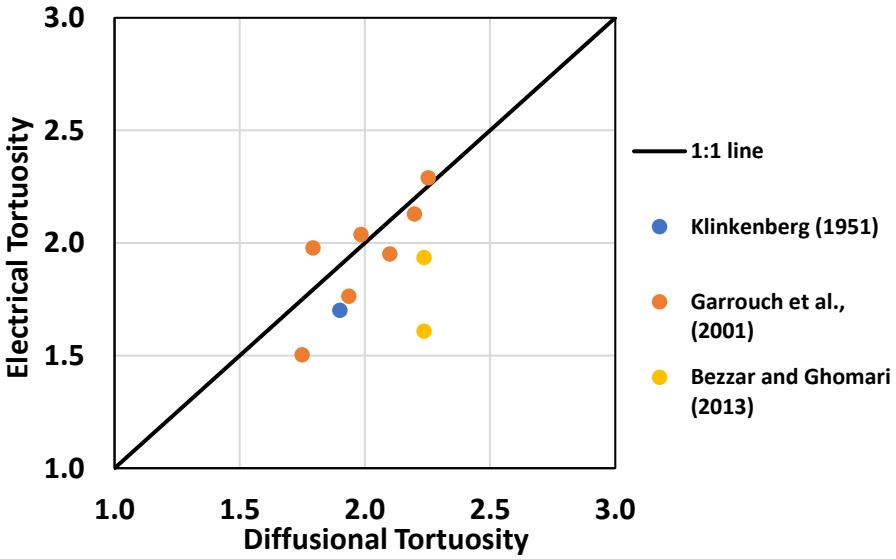

Figure 2-14. Comparison between electrical and diffusional tortuosity showing comparable results for synthetic consolidated core, Klinkenberg (1951), sandstones, Garrouch et al., (2001), Bezzar and Ghomari (2013) argue that both measures are different.

Clennell (1997) examined the relationship between electrical and chemical diffusive flows based on the assumptions that ion transport through pore space uses volume and time-averaged flux in a 1-dimensional case. By deriving relationships of current flow in terms of potential gradient and diffusive flux density in terms of concentration gradient, it was shown that the respective ratios of the bulk fluid phase conduction and diffusion to the effective pore conduction and diffusion are

identical. Martys et al., (1994) showed through numerical solutions of flow patterns in a 2-dimensional model with 75% porosity that the flow patterns of both electrical and diffusional flows are identical.

van Brakel & Heertjes (1974) postulated that the tortuosity in both cases might be different due to the chemical activity of sediment particles. These differences which may exist between the diffusional and electrical tortuosity have been attributed to secondary phenomena relating to solid-phase conduction, reactions between the diffusing solute and solid phase, anion exclusion, and the formation of a diffuse double layer where diffusion is slowed by electrokinetic drag and electric conductivity is enhanced by higher charge density (Clennell, 1997; Ghanbarian et al., 2013).

Chapter 3 : Experimental Methods and Samples Description

3.1 Experimental Methods

3.1.1 Mercury Injection Capillary Pressure

Mercury Injection Capillary Pressure (MICP) quantifies the amount of mercury intruded into a sample at different pressure steps. Our MICP experiments were conducted on circular rock samples that weighed between 8 - 12 g. The rock samples were dried at 100°C for a minimum of 12 hours and placed in a desiccator to cool before beginning measurements.

The prepared sample is placed in a penetrometer (glass sample holder with a stem) and introduced into the low-pressure system of a Micrometrics Autopore IV. In this low-pressure system, mercury is injected through the stem of the penetrometer up to a pressure of 27 psi in 31 pressure steps. Upon completion of the low-pressure injection, the penetrometer containing the sample and mercury is placed in the high-pressure system of the instrument, where the mercury pressure is increased up to 60,000 psi in 132 pressure steps.

Mercury is non-wetting to most materials; thus, mercury intrusion in the pore space will be controlled by the pore throat size as demonstrated by the Washburn equation (Eq 3.1).

$$r_{th} = 1.45 * 10^{-5} * \frac{2\gamma \cos\theta}{P_c} \quad (3.1)$$

Where the pore throat radius r_{th} is in cm, Pc is the corresponding capillary pressure in psi, γ is the interfacial tension (dyne/cm) for the system air-Hg (480 dyne/cm), and ϴ is the contact angle (140°) and $1.45 * 10^{-4}$ is the conversion factor from N/m^2 to psi.

MICP is used in determining the pore throat size distributions. Assuming a cylindrical pore structure, the average pore throat radius is given as:

$$r = \frac{2V}{A} \tag{3.2}$$

where V is the volume in m^3, and A is the surface area in m^2.

3.1.2 Subcritical Nitrogen Adsorption Experiments

Subcritical nitrogen adsorption experiments measure the amount of adsorbed nitrogen as a function of pressure at -196° C. For this study, our measurements were conducted on crushed rock samples (7 - 8 mm) weighing between 1-1.5 g which had been dried at 100°C under vacuum for 12 hours and placed in a chamber with nitrogen gas injected into the samples at low-pressure steps up to a relative pressure of 1.

Nitrogen gas adsorption experiment in subsurface sciences is used for estimating specific surface area and pore size distribution. The pressure at which a gas will condense in porous media is governed by the size of the pores where the gas resides. This phenomenon known as capillary condensation can be predicted by the Kelvin equation (Eq 3.3).

$$\frac{RT}{V}\ln\left(\frac{P_0}{P}\right) = \frac{2\gamma \cos(\theta)}{w} \tag{3.3}$$

Where R is the universal gas constant in J/K mol, T is the temperature in K, V is the molar volume in m^3/mol, P_0 is the saturated vapor pressure in psi, P is the vapor pressure in psi, γ is the interfacial tension for the system, θ is the contact angle, and w is the width of the slit-shaped pores in nm.

The Kelvin equation shows that pressure required for nitrogen to condense reduces as the pore size reduces. This concept is used to generate a pore size distribution from the nitrogen gas adsorption data. However, in order to distinguish the gas intake due to adsorption from the gas intake due to capillary condensation, the density functional theory (DFT) algorithm was used to generate the

pore size distributions (Seaton & Walton, 1989; Do & Do, 2003). This DFT algorithm assumes that the pores have slit shapes.

The pore size distribution generated from subcritical nitrogen gas adsorption represents a combination of pore throat and pore body size distribution.

3.1.3 Scanning Electron Microscopy (SEM)

SEM is an imaging method that uses a beam of electrons at the surface of solid samples to generate an image of the surface of samples with a resolution that can reach up to 0.5–4 nm.

To prepare our samples for SEM imaging, the thin section is polished using sandpaper of increasing grit sizes (180, 400, 600, 800, 1200), then ion milled to prepare the sample surface to minimize artifacts to a nanometer scale. To prevent charging effects the samples were coated with a thin gold layer. This study used an FEI Helios 600 Nanolab Dualbeam FIB/SEM for imaging. Two hundred twenty-five tile sets measuring 136 µm X 136 µm on each sample were stitched together to obtain a representative elemental area.

The SEM images generated were analyzed using Avizo 9.0 to study the samples' texture and obtain a pore size distribution. The pore size distribution obtained from SEM images is more representative of pore body size distribution.

3.1.4 Total Organic Carbon Measurement

The total organic carbon (TOC) content of the samples was measured using the LECO^{TM} method. The LECO^{TM} method measures TOC by quantifying the IR signal of the organic content during combustion. The instrument used for our TOC measurements is a LECO 774 Series.

Before the TOC measurements, approximately 1 g of a crushed rock sample (of particle size <35 mesh sieve) is treated with 35% hydrochloric acid to remove inorganic carbonates from the sample.

The acidized sample is rinsed with deionized water to remove the acid residues leftover during acidization. The sample is then dried at 100°C for 15 minutes before being placed into the LECO C844 carbon analyzer.

3.1.5 Fourier Transform Infrared Spectroscopy (FTIR)

During Fourier transform infrared (FTIR) measurements, a polychromatic light is transmitted through the sample, and the amount of energy lost at different frequencies due to vibration of the molecular bonds at a particular wavenumber is detected. This energy loss, termed the total absorbance, depends on the type and amount of minerals present and the sample thickness. For this thesis, the transmission FTIR measurements were conducted in the mid IR range (4000 – 400 cm^{-1}).

The samples for mineralogy quantification are crushed into fine particles, dried, and oxidized in a low-temperature plasma asher to remove organic matter. The ashed samples are then placed in a 100°C oven for a minimum of 4 hours. To begin measurements, 0.3g of potassium bromide (KBr) is made into a 1mm thick disc when placed under vacuum compression. This is used as a background measurement because it does not have vibration frequencies in the mid-infrared range.

0.0005g of the sample is mixed with 0.3g of KBr and vacuum compressed into a 1mm pellet. The pellet is then placed inside the Nicolet 6700 FTIR instrument for analysis.

Beer's law relates the total absorbance due to energy loss to the minerals present and their amount Eq. (3.4).

$$A = \sum_{i=1}^{n} \varepsilon_i l C_i \tag{3.4}$$

Where A is the total absorbance, ε_i is the absorptivity of the ith mineral, l is the optical path length, C_i is the concentration of the ith mineral. A spectroscopy library containing the spectra of minerals at different concentrations is used to identify and quantify mineralogy (Sondergeld and Rai, 1993; Ballard, 2007).

3.1.6 Nuclear Magnetic Resonance (NMR)

Nuclear Magnetic Resonance (NMR) measures the magnetic properties of nuclei exposed to an external magnetic field. For our applications, the properties of hydrogen nuclei at 12 MHz was focused upon.

Several types of NMR measurements can be conducted depending on how the external magnetic field is applied. For this thesis, I have performed CPMG (Carr-Purcell-Meiboom-Gill) and FID (free induction decay) measurements on brine saturated samples.

CPMG measurements provide T_2 distributions, which can be converted into pore body size distribution with Eq 3.5 (**Figure 3-1**). The average pore body radius obtained from the NMR pore size distribution is given as

$$r = 2\rho T_2 \tag{3.5}$$

Where r is the pore body radius, ρ is the surface relaxivity (μm/s), T_2 is the geometric average T_2 relaxation time is given as

$$T_2 = \left(\prod_{1}^{n} T_{2i}^{\ \emptyset_i} \right)^{\frac{1}{\emptyset_t}} \tag{3.6}$$

Where $T_2 i$ is the incremental T_2 relaxation time associated with a pore radius, $\emptyset_i$ is the NMR incremental porosity corresponding to the T_2 relaxation time and $\emptyset_t$ is the cumulative porosity.

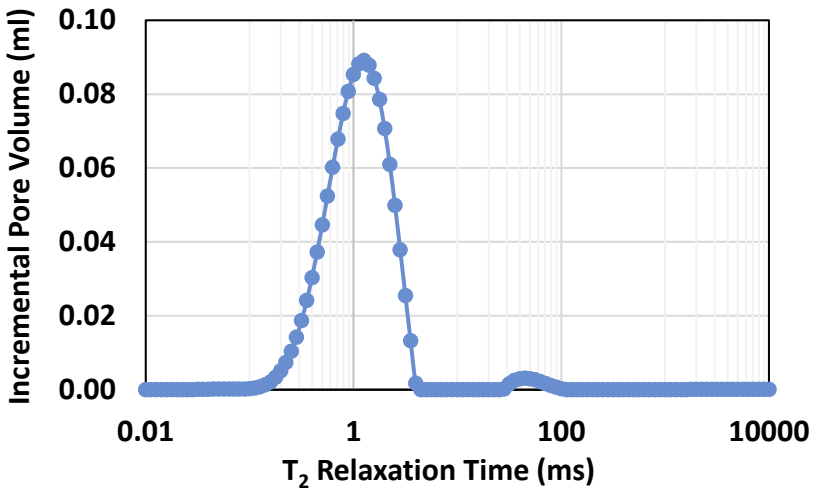

Figure 3-1. NMR pore body size distribution.

FID measurements can be used to measure the total ^{1}H based fluid content in a sample, while T_2 measurements can be used to measure both the fluid content in the sample and characterize a sample's pore structure. However, in this study, FID measurements were used to measure the water volume in the sample because they are relatively faster than T_2 measurements. Based on our NMR parameter settings, the FID measurements can be run in 12 seconds, while the T_2 measurements take 8 minutes to complete.

3.1.7 Resistivity Measurements

The electrical resistivity measurements were conducted with a 2-electrode system using an LCR (inductance, capacitance, resistance) meter. The sample is placed between a bar clamp with two-plate parallel capacitors, as shown in **Figure 3-2**. The coupling between the sample surface and electrode was improved by placing a wet paper filter saturated with the same brine solution in the

core sample between the sample surface and electrodes. The bar clamp allows the sample to be in tight contact with the electrodes while taking impedance measurements.

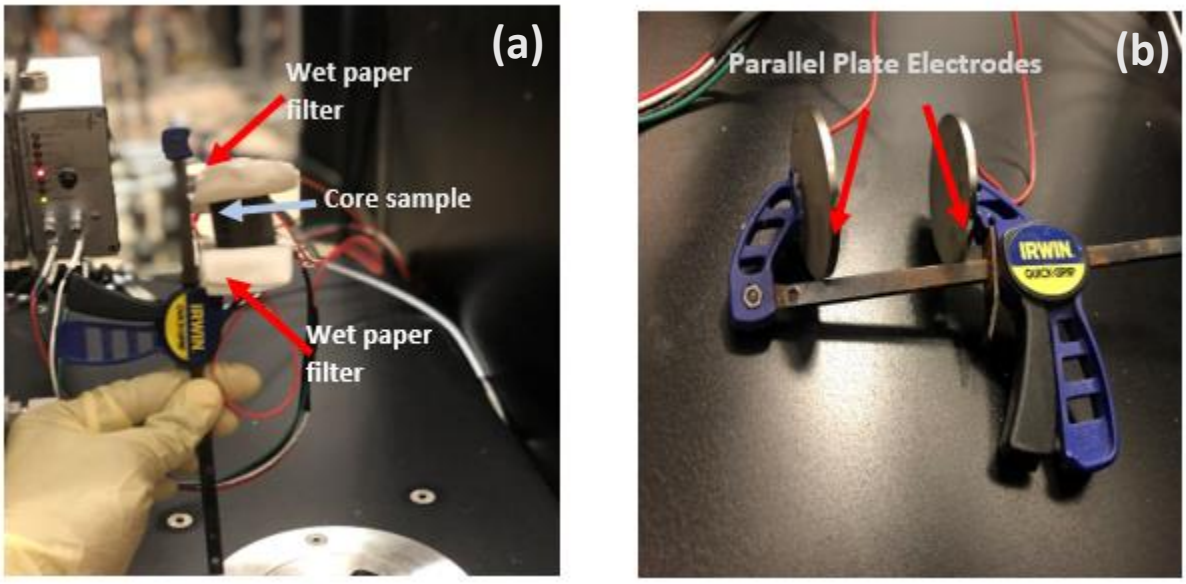

Figure 3-2. 2-electrode system to measure the resistivity of the core sample. (a) A wet paper filter is used to prevent polarization effects at the sample-electrode interface. (b) Experimental setup showing the 2-electrode system in parallel before measurements.

Alternating current is passed through the sample, and the time-varying voltage is measured. The phase of the received voltage, called polarization was calculated using the current waveform as a reference.

$$Z^* = |Z|e^{i\varphi} = Z' + iZ'' \tag{3.7}$$

Where Z' is the real part of the complex impedance in ohms (Ω), Z'' is the imaginary part of the complex impedance in ohms (Ω). The complex impedance was recorded along 10 logarithmically distributed points between 100 Hz and 100,000 Hz. From the known voltage and current, the resistance across the core can be determined, and the electrical resistivity is calculated Eq. (3.8):

$$R = \frac{A}{L}Z \tag{3.8}$$

Where R is the resistivity (ohm-meter), A is the cross-section area of the core sample (m^2), L is the length of the core sample (m), and Z is the real component of the measured impedance in ohms(Ω).

3.1.8 Dielectric Measurements

The pore-filled brine salinity was measured using the dielectric method based on the principle of frequency-dependent dielectric loss dispersion (Odiachi et al., 2021). **Figure 3-3** shows the frequency-dependent dielectric loss response in bulk saline solutions.

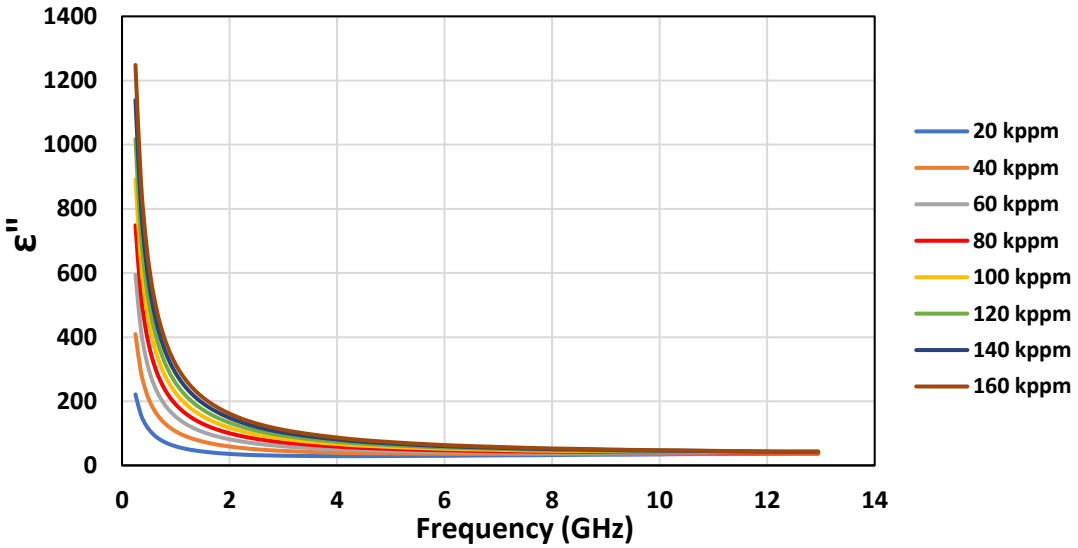

Figure 3-3. Relationship between dielectric loss and frequency for bulk NaCl brine solutions ranging from 20 kppm – 160 kppm (2-16 wt.%). The loss ratio is determined as the ratio of the dielectric loss at low and high frequencies of 2.05 GHz and 11.05 GHz respectively.

The cylindrical core plugs measuring 1 inch by 1 inch were placed directly under a dielectric probe to measure the dielectric loss response in the sample and determine the loss ratio. The loss ratio is the ratio of dielectric loss at 2.05 GHz and 11.05 GHz and it is directly related to the pore fluid salinity (**Figure 3-4**).

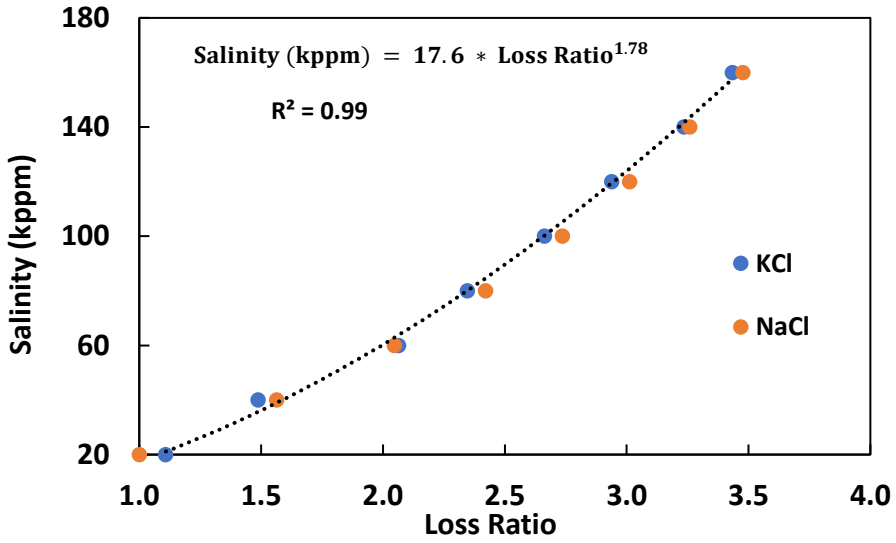

Figure 3-4. Calibration curve showing the relationship between pore fluid salinity and loss ratio for NaCl and KCl bulk brine solutions at 21°C. The calibration curve shows comparable results for NaCl and KCl bulk brine solutions Odiachi et al., (2021).

The predicted pore-filled brine salinity from the loss ratio is then used in determining the water resistivity.

3.2 Samples Description

The present study was conducted on twelve tight rock samples collected from the Utica, Middle Bakken, Eagle Ford, and Wolfcamp formations. In addition to the toght rock samples, three sandstone samples from the Berea formation, Lyon formation, and Illinois Basin, a coal-bearing formation (Hatch et al., 2002), were used as control samples.

The tight rock samples and the Illinois Basin sandstone were downhole samples, while the Berea and Lyon sandstones were outcrop samples.

Table 3-1 presents a summary of the petrophysical properties of the samples used in this study. The Eagle Ford samples are from the oil window with a porosity varying from 8 - 13.5%, TOC varying from 1.42 – 6.20%, and clay content varying from 21 - 43%. The Wolfcamp samples are from the oil window with a porosity ranging from 7.4 - 13.7%, TOC ranging from 1.83 – 3.73%, and clay content ranging from 9.6 – 28.2%. The Utica sample has a porosity of 10.8%, 0.86% TOC, and 70.7% clay content. The Bakken samples are from the immature window with porosity between 4.5 – 12.9%, TOC between 0.13 - 0.35%, and clay content between 9.6 – 28.2%. The sandstone samples had porosity varying from 5.7 – 19%, TOC varying from 0.02 - 2.3%, and clay content varying from 5 - 18.5%.

Table 3-1: Summary of the petrophysical properties of the samples used in this study.

Formation	Sample	Porosity (%)	TOC (wt.%)	Clay Content (wt. %)	Quartz + Feldspar (wt. %)	Carbonate (wt. %)
Eagle Ford	EF 1	13.13	6.00	21.0	16.0	59.0
	EF 2	13.50	6.20	32.0	8.0	57.0
	EF 3	11.43	6.12	31.5	5.9	59.6
	EF 4	7.97	1.42	43.0	3.0	52.0
Wolfcamp	WC 1	13.71	3.38	28.2	67.0	5.1
	WC 2	7.94	1.83	15.0	37.6	45.3
	WC 3	7.38	3.73	9.6	74.1	16.0
Utica	UT 1	10.79	0.86	70.7	26.2	1.0
Bakken	BK 1	4.47	0.19	18.0	49.0	33.0
	BK 2	12.94	0.13	47.0	23.0	29.0
	BK 3	8.36	0.31	3.0	24.0	72.0
	BK 4	7.86	0.35	15.0	26.0	59.0
Berea	Berea SS	18.87	0.02	5.0	90.8	3.6
Lyon	Lyon SS	5.72	0.04	10.0	85.0	5.0
Illinois Basin	ILB	7.90	2.30	18.5	76.8	4.7

Figure 3-5 shows that the main pore throat radii for the tight rock samples are below 20 nm, while the sandstones have large pore throats in the micrometer range (0.1 – 3 μm).

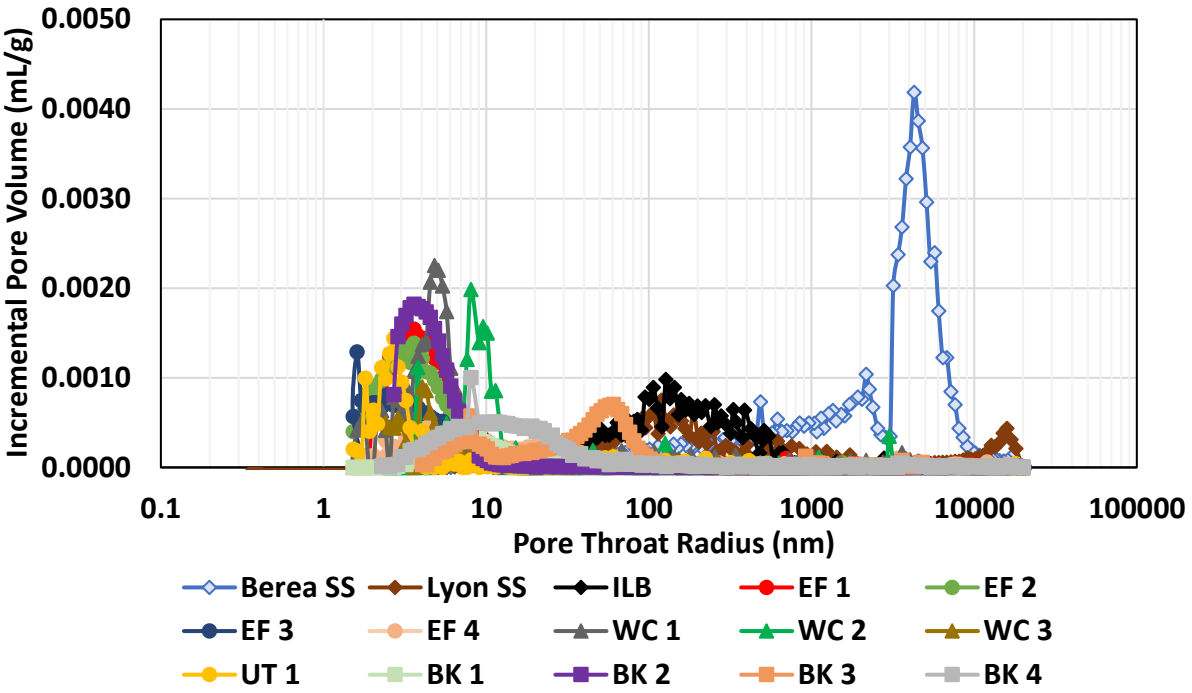

Figure 3-5. Mercury injection capillary pressure measurements of the samples used in this study. The samples from the Eagle Ford, Wolfcamp, Utica, and Bakken formations appear tighter with pore throats < 20nm except for BK3, which shows a bimodal pore throat size distribution compared to the sandstones from Berea, Lyon, and Illinois Basin, which have pore throat sizes in the micrometer range.

The pore body size distributions were obtained from SEM image analysis and subcritical nitrogen adsorption measurements.

Figures 3-6 and **3-7** indicate that samples from the Eagle Ford and Wolfcamp formations show the presence of water-wet pores (T_2 < 1ms) and oil-wet pores (T_2 > 1ms) while the sandstones and samples from the Utica and Bakken formations have a unimodal pore system.

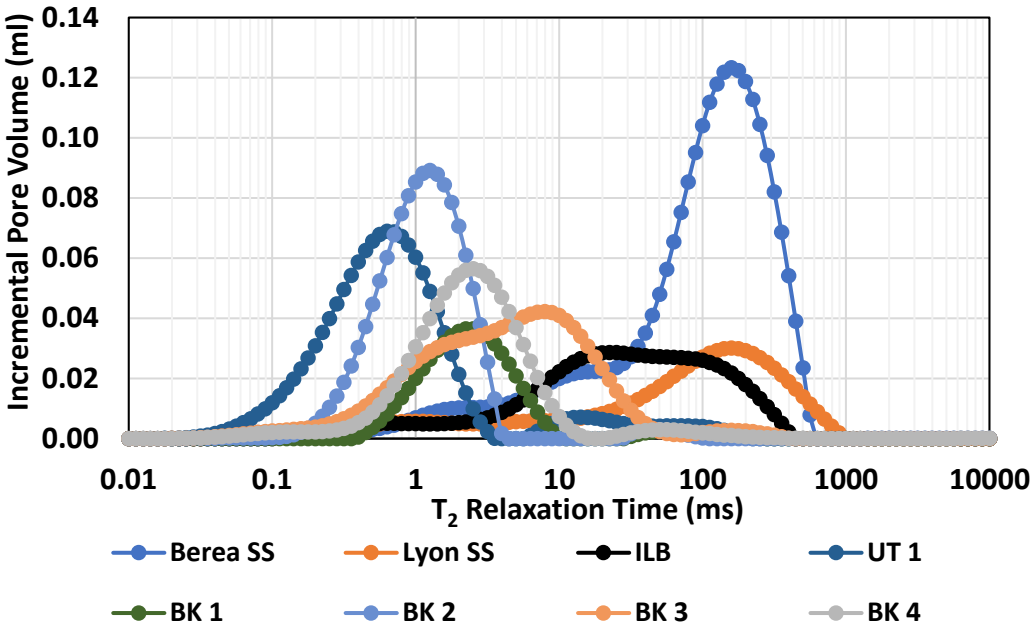

Figure 3-6. NMR T_2 distribution on the sandstone samples and samples from the Utica and Bakken formations with one distinct peak, indicating a unimodal pore system. The sandstone samples show bigger pore sizes, as shown by their longer T_2 relaxation times.

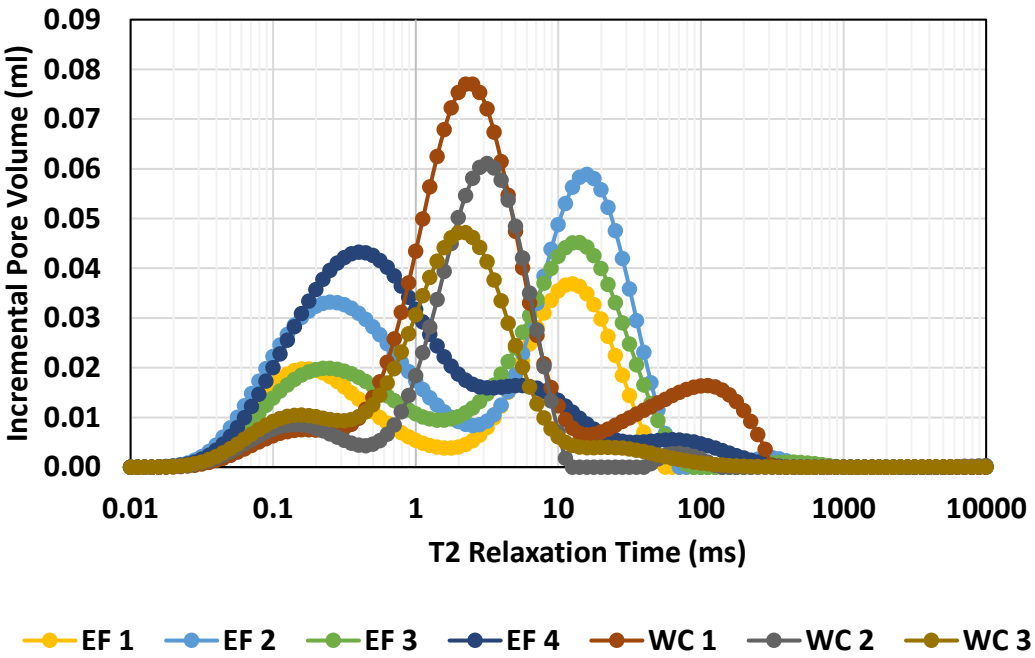

Figure 3-7. NMR T_2 distribution on samples from the Eagle Ford and Wolfcamp formations with two peaks, indicating the presence of water-wet (T_2 < 1ms) and oil-wet pores (T_2 > 1ms).

SEM images were acquired on eight tight rock samples. **Figures 3-8** to **3-14** show that the samples from the Bakken formation have large grain sizes with no organic matter. It is also observed that the pores are hosted in the inorganic matrix. The Wolfcamp samples show the presence of both inorganic and organic matter hosted porosity with sample WC2 showing little presence of organic matter and WC3 sample has small-sized grains. The Eagle Ford samples show mostly the presence of organic hosted porosity and little amount of inorganic porosity with plate shaped, large grain sizes, while the sample from the Illinois basin shows high presence of high amount of organic matter (**Figures 3-8** to **3-14**).

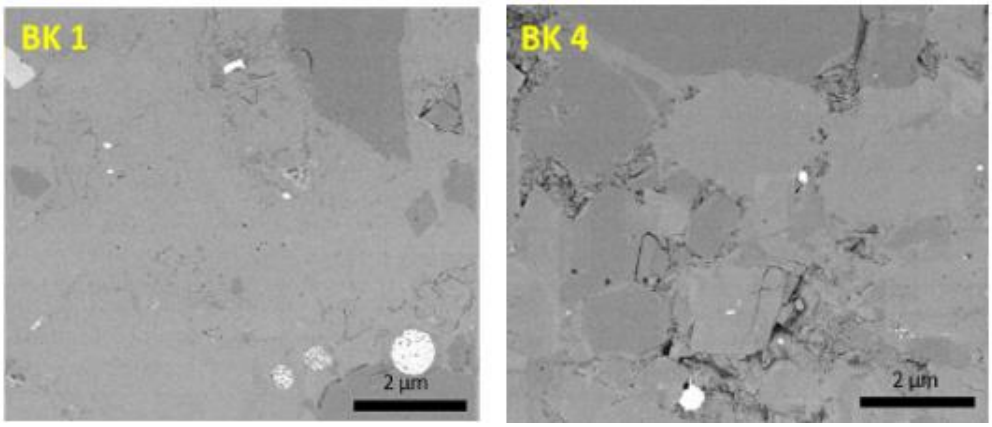

Figure 3-8. The Bakken samples show no organic matter. Grain size is quite large, with porosity in the smaller grains and clay between the larger grains.

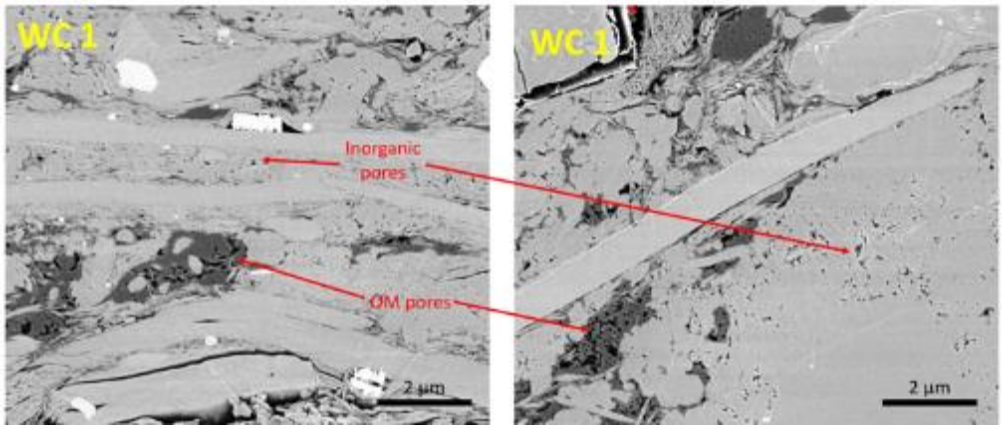

Figure 3-9. Wolfcamp sample showing the presence of inorganic and organic pore pathways. In the region between the large grains, organic matter and clay both show porosity.

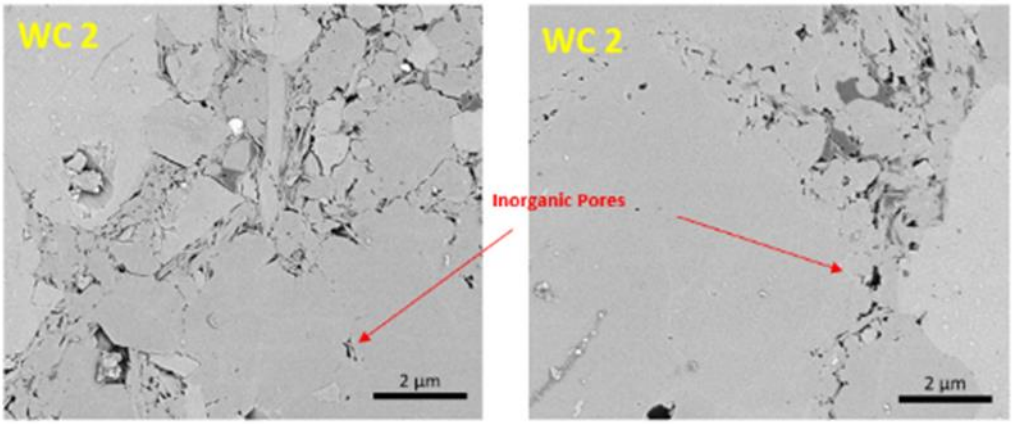

Figure 3-10. Wolfcamp sample showing very little organic matter. Most of the porosity occurs in the inorganic matrix.

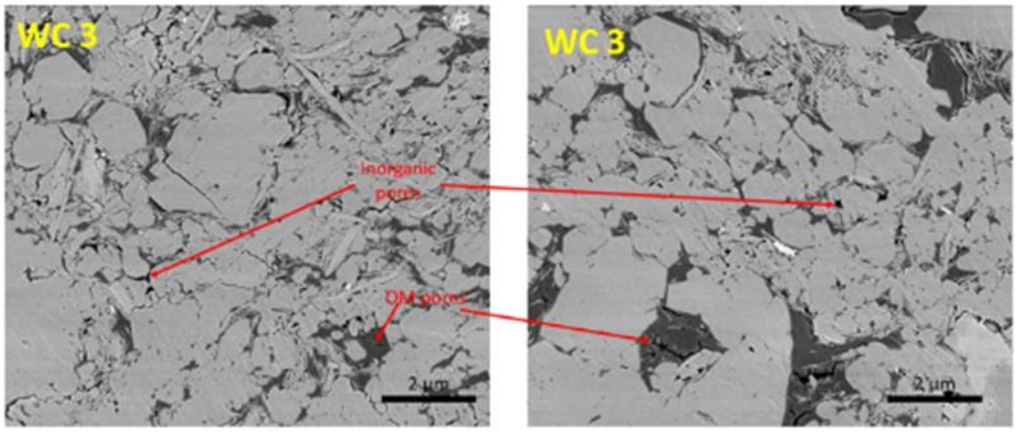

Figure 3-11. Wolfcamp sample showing the presence of organic matter with cracks and porosity. There is a presence of small-sized grains with intragranular porosity.

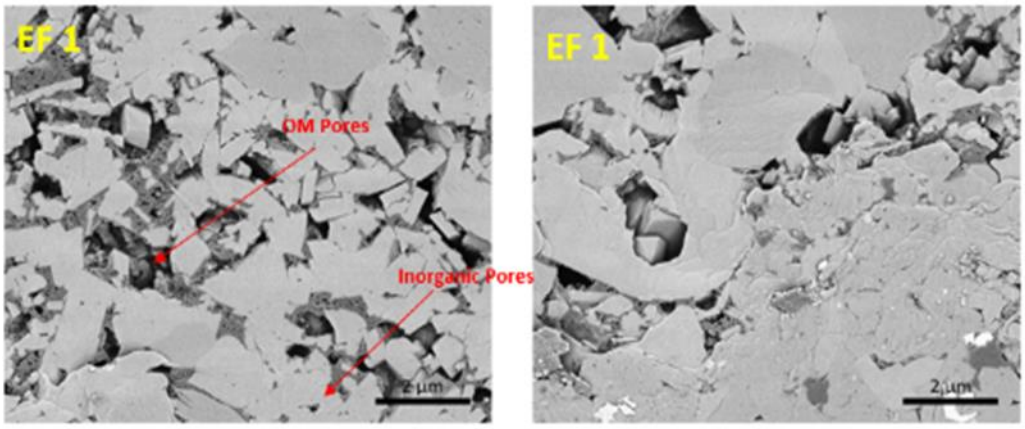

Figure 3-12. Eagle Ford sample showing the presence of both organic and inorganic hosted porosity.

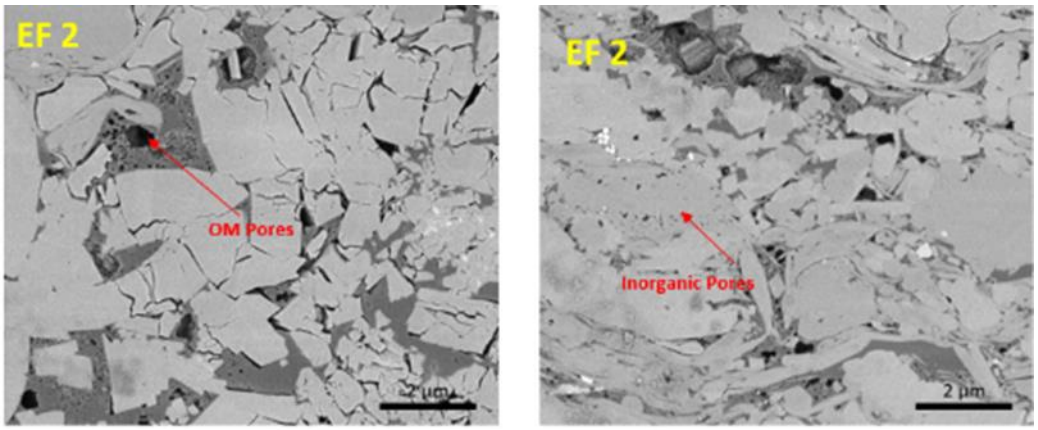

Figure 3-13. Eagle Ford sample showing the presence of organic and inorganic hosted porosity.

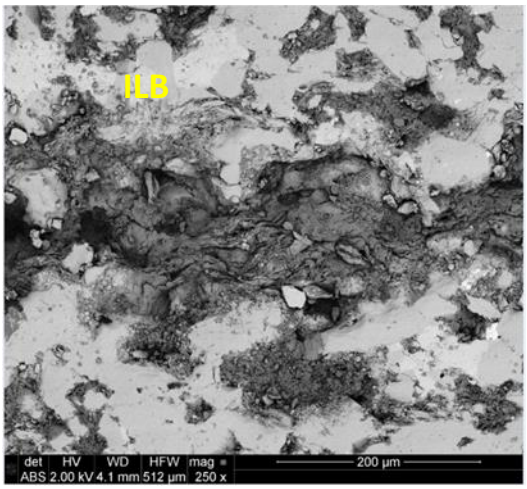

Figure 3-14. Illinois Basin sandstone shows a high amount of organic matter (coal), and organic matter hosted porosity.

Figure 3-15 illustrates the pore body radii distributions obtained from SEM image analysis. The samples show similar pore body radii distributions with pore sizes ranging from 5 – 3000 nm.

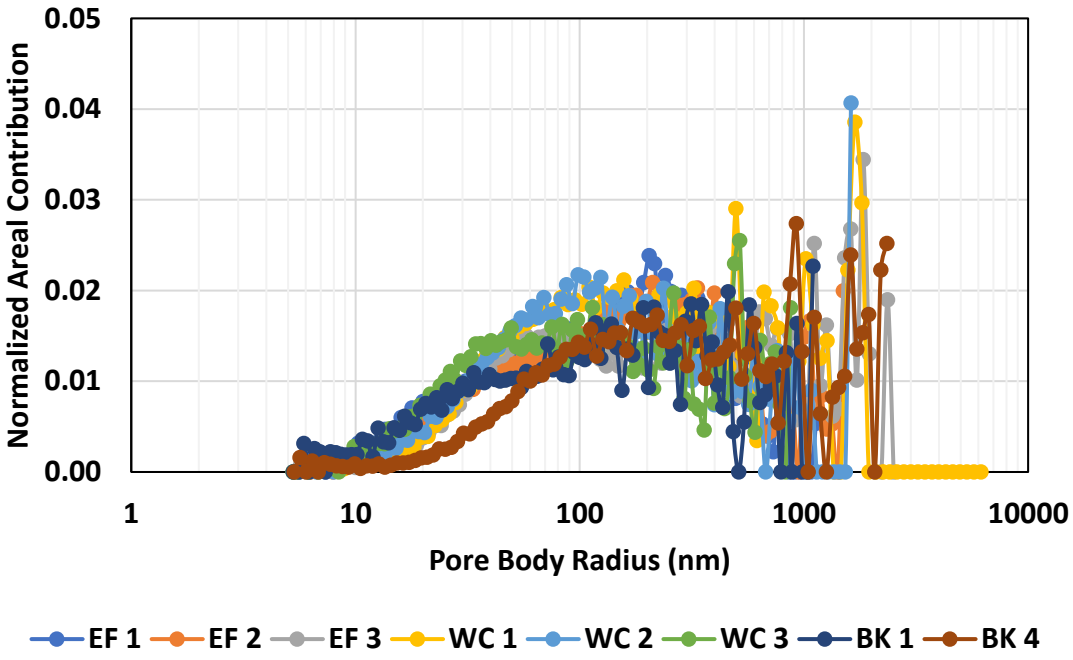

Figure 3-15. Pore body size distributions from SEM image analysis on eight of the twelve samples used in this study. Sample BK4 shows a smaller contribution of pores in the range 10 - 50 nm compared to other samples.

The pore body radius distributions were also obtained using subcritical nitrogen adsorption measurements (**Figure 3-16**). The results showed that the pore body radii ranged between 2 to 400 nm. However, the pore body size distributions obtained from subcritical nitrogen adsorption measurements were not used for further analysis in this study. This is because the SEM pore body size distribution, which considered eight of the twelve tight rock samples, shows that there are pore body radii greater than 300 nm, whereas the pore body radii obtained from subcritical nitrogen adsorption measurements are generally below 300nm.

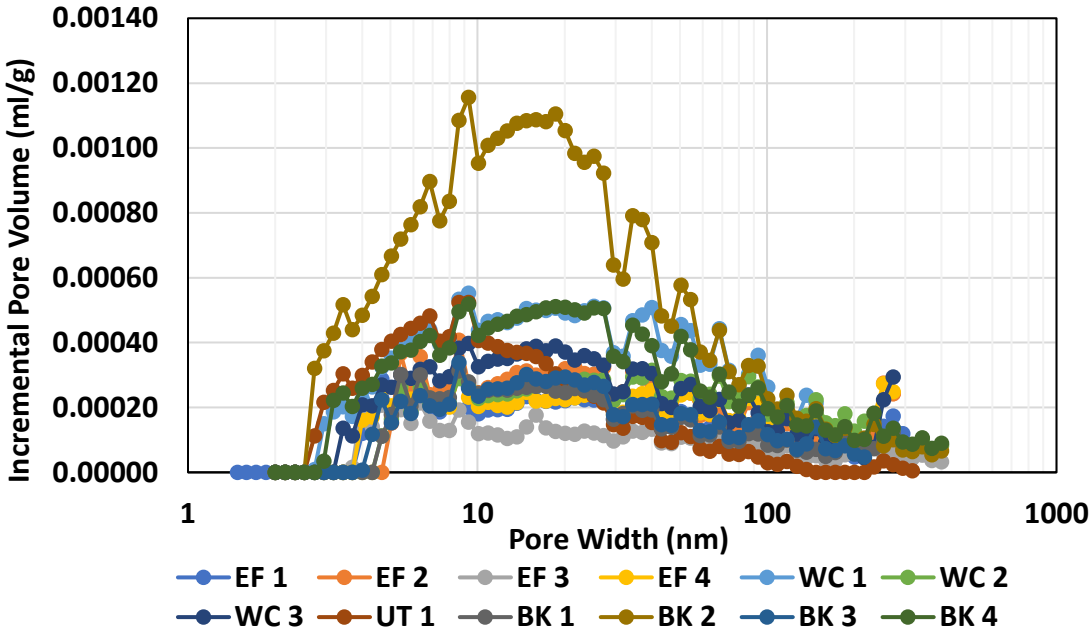

Figure 3-16. Pore body size distributions from subcritical nitrogen adsorption measurements for the tight rock samples used in this study from Eagle Ford, Wolfcamp, Utica, and Bakken formations. Sample BK2 shows a larger incremental pore volume contribution of pore width in the 5 - 100 nm range compared to other samples.

3.3 Experimental Workflow

Figure 3-17 shows the general experimental workflow used in this study. After sample preparation which included sample cleaning, drying and saturation, the diffusional tortuosity measurements begin with sample immersion in D_2O and end at NMR measurement as a function of time, while the electrical tortuosity measurements begin with resaturating the sample in 25,000ppm KCl brine for 96 hours to give time for the D_2O in the samples to diffuse out and 25,000ppm KCl brine diffuse into the sample, then immersing the sample into 60,000ppm KCl brine to begin ionic diffusion.

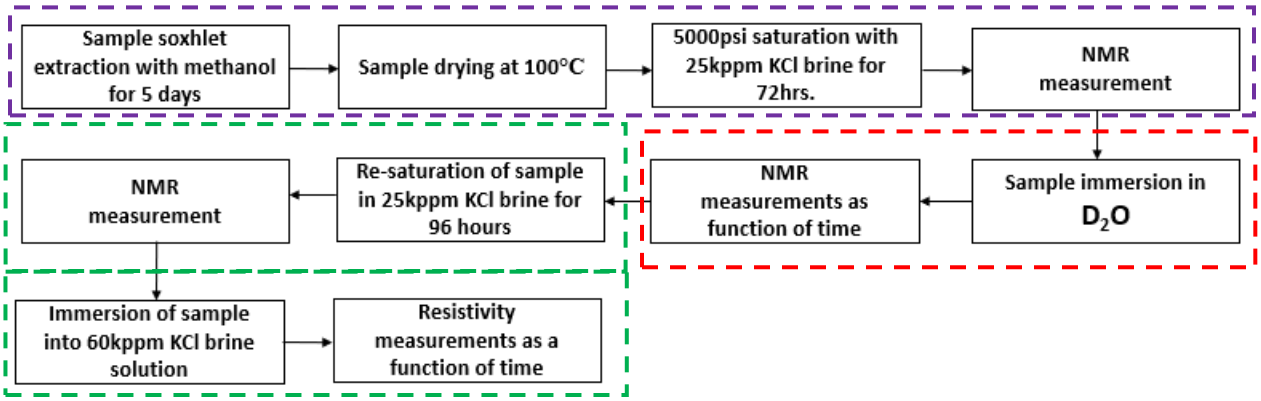

Figure 3-17. Experimental workflow used in the present study. The purple dashed rectangle represents the workflow before diffusional tortuosity experiments, the red dashed rectangle represents the workflow for diffusional tortuosity measurements and the green dashed rectangle represents the workflow for electrical tortuosity measurements.

Chapter 4 : Tortuosity and Effective Porosity Measurements

4.1 Diffusional Tortuosity Measurements

4.1.1 Experimental Procedure for Diffusional Tortuosity Measurements

For the tortuosity experiments, I have prepared 1-inch by 1-inch core plugs of the samples described in section 3.2. These core plugs were soxhlet-extracted with methanol and dried at 100°C in a convection oven until their weights stabilized. The drying step was followed by the saturation of the samples with 25,000 ppm KCl brine for 72 hours.

Upon saturation, the samples were immersed in a D_2O solution with 25,000 ppm KCl at room temperature (23 $\pm$ 2°C) to allow the diffusion of D_2O into the samples and the diffusion of H_2O out of the samples (**Figure 4-1**). The D_2O-H_2O diffusion process was monitored as a function of time with 12 MHz NMR FID measurements.

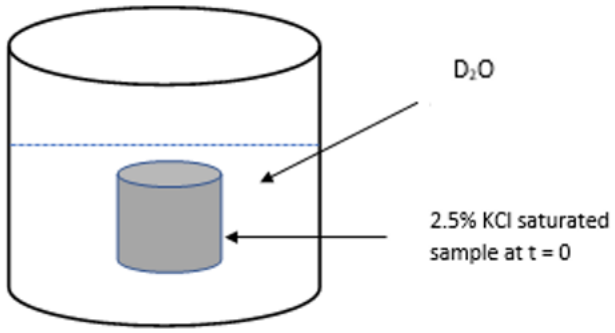

Figure 4-1. Schematic representing a core sample initially saturated with 25,000 ppm KCl brine solution immersed into a D_2O solution. While the sample is immersed in D_2O, H_2O will diffuse out of the sample, and D_2O will diffuse into the sample.

4.1.2 Computation of Effective Pore Fluid Diffusion Coefficient

12 MHz NMR FID measures the volume of H_2O in the sample. Therefore, the measured NMR FID volume is expected to reduce as a function of time because D_2O does not have an NMR signal. The change in NMR FID volume as a function of time represents the change in the H_2O concentration related to the effective pore fluid diffusion coefficient.

To compute the effective pore fluid diffusion coefficient, it is assumed that diffusion occurs radially and along the length of the sample (Crank, 1975; Fleury et al., 2020). The concentration change of hydrogen molecules due to diffusion along the length of the sample can be modeled using Eq. (4.1) (Crank, 1975).

$$C_l = \sum_{n=1}^{\infty} \frac{2\alpha(1+\alpha)}{1+\alpha+\alpha^2 {p^2}_n} \exp(-D_{eff} * {p^2}_n * \frac{t_D}{l^2}) \tag{4.1}$$

where C_l is the H_2O concentration remaining in the sample due to diffusion along the length of the sample, α is the ratio of D_2O over H_2O, p_n represents the non-zero positive roots of Eq. (4.2):

$$tan\, p_n = -\alpha p_n \tag{4.2}$$

D_{eff} is the effective pore fluid diffusion coefficient, t_D is the diffusion time, l is the length of the sample.

To model the concentration change of H_2O due to diffusion radial diffusion, Eq. (4.3) was used

$$C_r = \sum_{n=1}^{\infty} \frac{4\alpha(1+\alpha)}{4+4\alpha+\alpha^2 {q^2}_n} exp\left(-D_{eff} * {q^2}_n * \frac{t_D}{r^2}\right) \tag{4.3}$$

where C_r is the H_2O concentration remaining in the sample due to diffusion along the radius of the sample, q_n represents the non-zero positive roots of Eq. (4.4):

$$\alpha q_n J_0(q_n) + 2J_1(q_n) = 0 \tag{4.4}$$

where J_0 and J_1 are the Bessel function of the first type of order 0 and 1 respectively, and r is the radius of the sample.

To compute the effective pore fluid diffusion coefficient, the total H_2O concentration remaining in the sample was modeled according to Eq. (4.5).

$$C^* = \frac{M(t) - M(t = \infty)}{M(t = 0) - M(t = \infty)} = C_l * C_r \tag{4.5}$$

Where C^* is the normalized time-dependent H_2O concentration, $M(t)$ represents NMR FID volume at time t, $M(t = 0)$ represents NMR FID volume at t = 0, and $M(t = \infty)$ represents the NMR FID volume at the end of diffusion.

The effective pore fluid diffusion coefficient is obtained by matching the experimental data with the model from Eq. (4.5) (**Figure 4-2**).

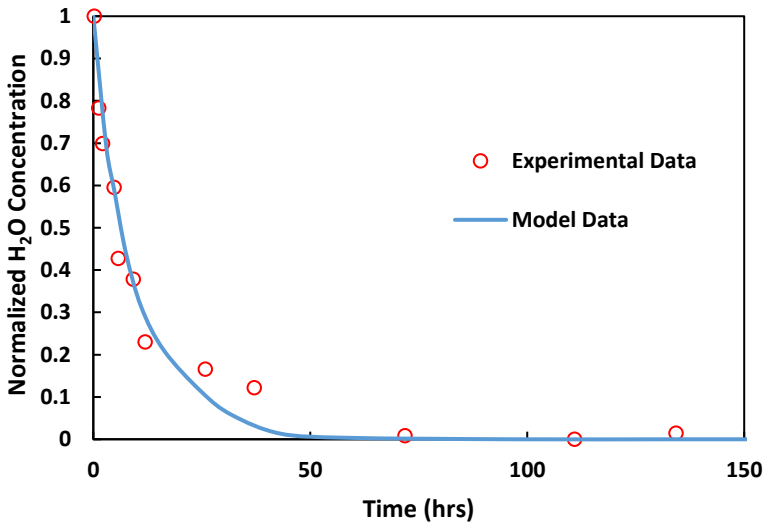

Figure 4-2. Model and experimental data of the H_2O concentration as a function of time in sample BK1. The sample's effective pore fluid diffusion coefficient can be determined by fitting the model data to the experimental data.

The computation of C_l and C_r requires a minimum number of terms in the series. To determine the optimal number of terms, the effective pore fluid diffusion coefficient was computed as a function of number of terms. The point at which the effective pore fluid diffusion coefficient remained constant irrespective of the number of terms used in the series is the optimal number of terms used in computing C_l and C_r. **Figure 4-3** shows that the optimal number of terms required to compute C_l and C_r in Bakken sample BK1 is 4. Therefore, four terms were used for the computation of C_l and C_r.

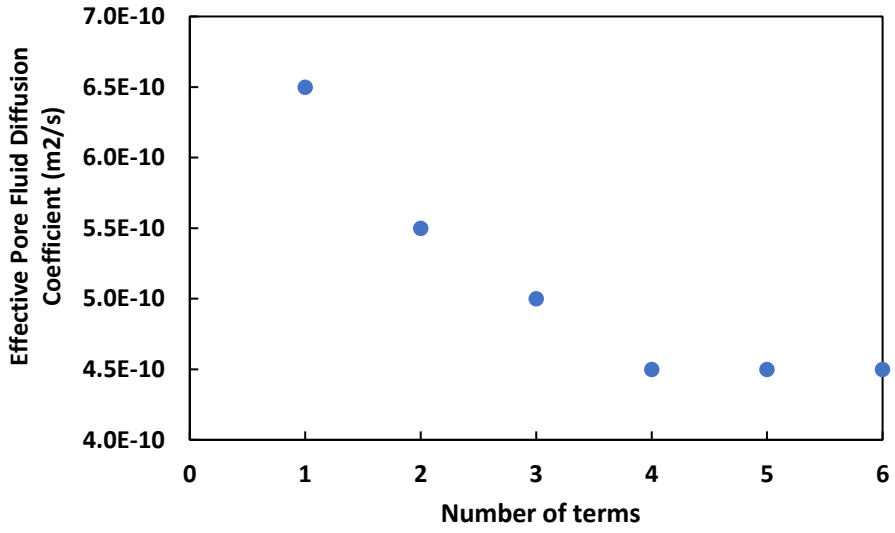

Figure 4-3. Determination of number of terms to be used in plane sheet and cylinder diffusion model to determine effective pore fluid diffusion coefficient for sample BK1.

Figure 4-4 shows that the effective pore fluid diffusion coefficients for the Eagle Ford samples varied between $7.5*10^{-11}$ to $4.6*10^{-10}$ m^2/s. The effective pore fluid diffusion coefficients for the Wolfcamp samples varied between $1.6*10^{-10}$ to $4.2*10^{-10}$ m^2/s. The effective pore fluid diffusion coefficients for the Bakken samples varied between $3.5*10^{-10}$ to $6.2*10^{-10}$ m^2/s. The Utica sample had an effective pore fluid diffusion coefficient value of $4.8*10^{-10}$ m^2/s while the effective pore fluid diffusion coefficients for the sandstone samples varied between $1.4*10^{-10}$ m^2/s to $1.1*10^{-9}$ m^2/s.

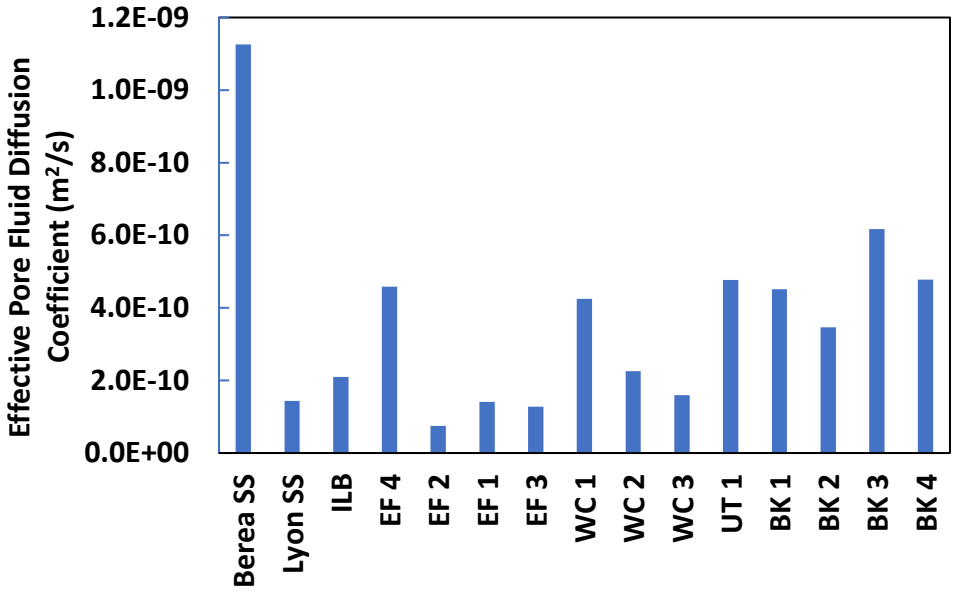

Figure 4-4. Effective pore fluid diffusion coefficient values for the samples used in the study. The Berea sandstone shows the largest effective pore fluid diffusion coefficient value while the Eagle Ford samples have the lowest effective pore fluid diffusion coefficient values.

4.1.3 Diffusional Tortuosity of Tight Rocks

The diffusional tortuosity of the samples was obtained from the square root of the bulk diffusion coefficient of D_2O over the effective pore diffusion coefficient Eq. (2.9). The bulk diffusion coefficient of D_2O is $2.3*10^{-9}$ m^2/s at 25°C (Baur et al., 1959; Mills, 1973; Meng et al., 2018). **Figure 4-5** shows that the diffusional tortuosity values for the Eagle Ford samples ranged from 2.2 to 5.4, the diffusional tortuosity values for the Wolfcamp samples ranged from 2.3 to 3.7, the diffusional tortuosity values for the Bakken samples ranged from 1.9 to 2.5, the Utica sample had a diffusional tortuosity value of 2.1 and the diffusional tortuosity values for the sandstone samples ranged from 1.4 to 3.9.

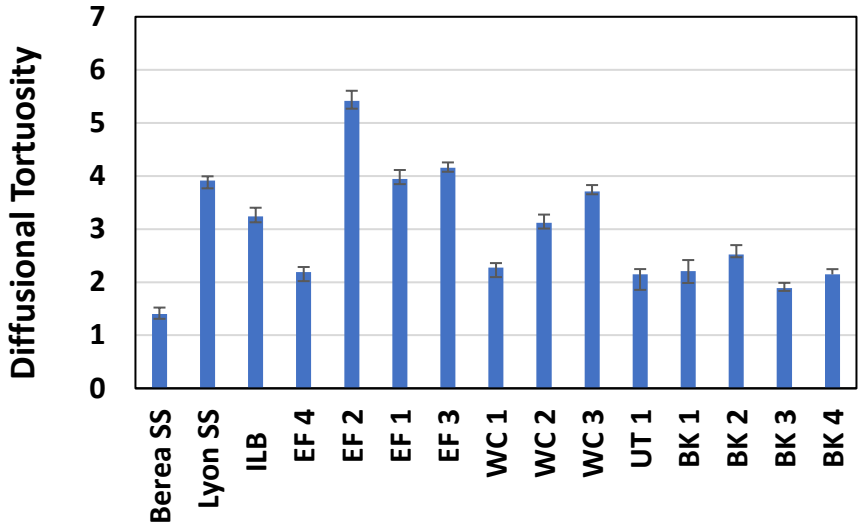

Figure 4-5. Diffusional tortuosity values for the samples used in the study. The Berea sandstone sample shows the lowest diffusional tortuosity, while the Eagle Ford samples have the largest diffusional tortuosity values.

4.2 Electrical Tortuosity Measurements

4.2.1 Experimental Procedure for Electrical Tortuosity Measurements

In reservoir rocks, electrical conductivity is generally due to the movements of ions contained in the saturating brine. To obtain the electrical tortuosity values, the diffusion of K^+ and Cl^- ions in the rock samples selected for this study have been measured.

Before the ionic diffusion measurements, the core plugs used for the diffusional tortuosity measurements were resaturated in 25,000 ppm KCl brine for 96 hours to allow D_2O to diffuse out of the sample. NMR volume measurements were then used to check that the samples contained 25,000 ppm KCl brine by comparing the current saturation volume with the previous saturation volume before diffusional tortuosity measurements. Upon saturation, the samples were immersed in 60,000 ppm KCl brine solution at room temperature (23 ± 2°C) to allow the diffusion of K^+ and

Cl^- ions from the brine solution to the sample containing 25,000 ppm KCl brine (**Figure 4-6**). Resistivity measurements monitored the ionic diffusion process as a function of time.

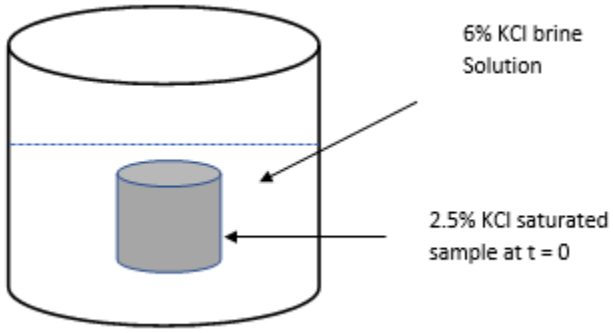

Figure 4-6. Schematic of a core sample saturated with 25,000 ppm KCl brine immersed in 6% KCl brine solution. It is expected that the brine concentration in the sample to increase from 25,000 ppm to 60,000 ppm over time.

4.2.2 Computation of Effective Pore Ionic Diffusion Coefficient

60,000 ppm KCl brine has a lower resistivity than 25,000 ppm KCl brine. Therefore, the measured resistivity on a given sample is expected to reduce as a function of time.

To compute the effective pore ionic diffusion coefficient, using the same approach detailed in section 4.1.2, it is assumed that the K^+ and Cl^- ions diffused into the sample along the length of the sample and radially.

Therefore, the normalized time-dependent brine concentration, Cs^* is given by:

$$Cs^* = \frac{R(t) - R(t = \infty)}{R(t = 0) - R(t = \infty)} = C_{sl} * C_{sr} \quad (4.6)$$

where $Ro(t)$ is the sample resistivity at time t, $Ro(t = 0)$ is the sample resistivity at the beginning of ionic diffusion, and $Ro(t = \infty)$ is the sample resistivity at the end of ionic diffusion, C_{sl} represents the KCl concentration resulting from diffusion along the length of the sample and C_{sr} represents the KCl concentration resulting from diffusion along the radius of the sample.

Figure 4-7 shows that the effective pore ionic diffusion coefficients are determined by matching the experimental data with the model data from Eq. (4.6).

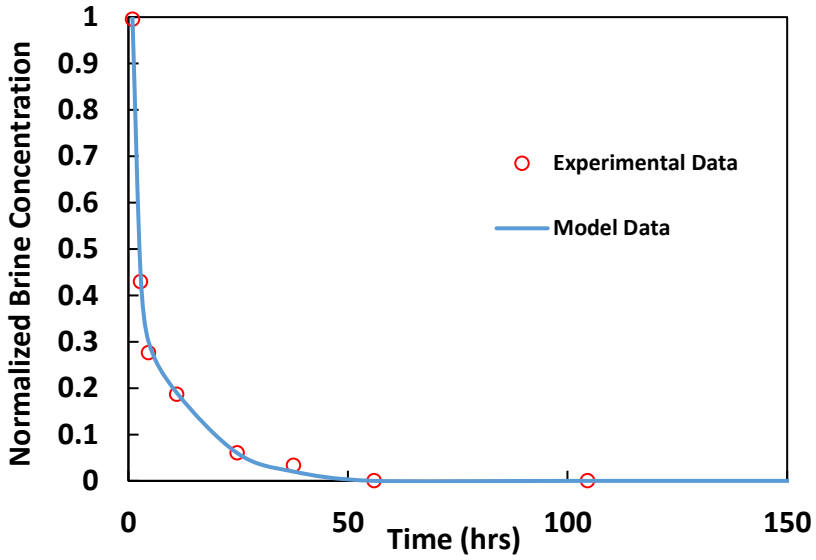

Figure 4-7. Model and experimental data of the KCl brine concentration as a function of time in sample BK1. The effective pore ionic diffusion coefficient of the sample can be determined by fitting the model data to the experimental data.

Figure 4-8 shows that the effective pore ionic diffusion coefficients for the Eagle Ford samples varied between $5.5*10^{-11}$ to $4.1*10^{-10}$ m^2/s. The effective pore ionic diffusion coefficients for the Wolfcamp samples varied between $8.5*10^{-11}$ to $4.3*10^{-10}$ m^2/s. The effective pore ionic diffusion coefficients for the Bakken samples varied between $5.0*10^{-10}$ to $6.5*10^{-10}$ m^2/s. The Utica sample had an effective pore ionic diffusion coefficient value of $4.5*10^{-10}$ m^2/s and the effective pore ionic diffusion coefficients for the sandstone samples varied between $1.4*10^{-10}$ m^2/s to $8.0*10^{-10}$ m^2/s.

The Berea sample has the highest effective pore ionic diffusion coefficient while the Eagle Ford samples have the lowest effective pore ionic diffusion coefficient values similar to observations from the effective pore fluid diffusion coefficient.

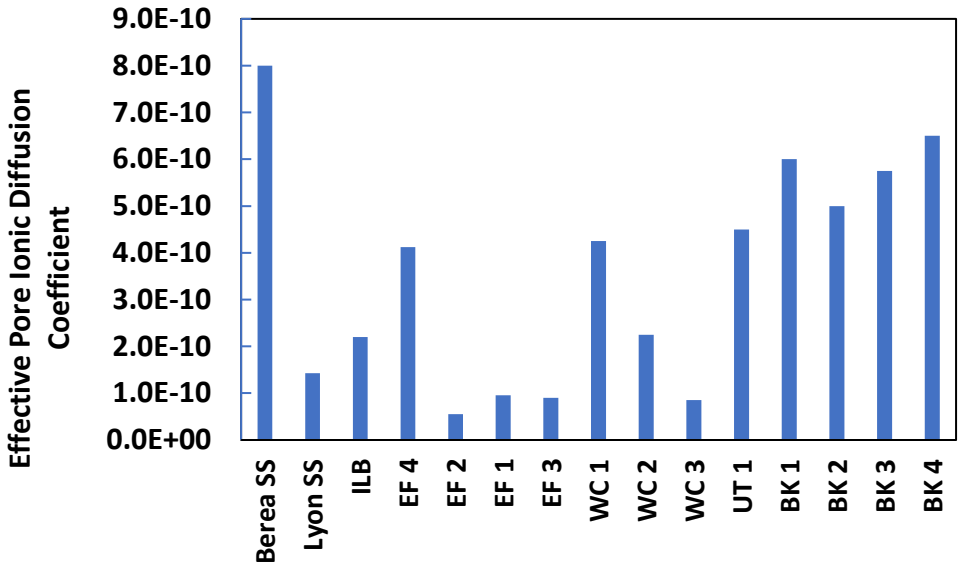

Figure 4-8. Effective pore ionic diffusion coefficient values for the samples used in the study. The Berea sandstone has the largest effective pore ionic diffusion coefficient value, while the Eagle Ford samples have the lowest effective pore ionic diffusion coefficient values.

4.2.3 Electrical Tortuosity of Tight Rocks

The electrical tortuosity is obtained from the ratio of the square root of the bulk ionic diffusion coefficient over the sample's effective pore ionic diffusion coefficient (Eq. 2.11). The bulk ionic diffusion coefficient used in our calculations is 1.9 $*10^{-9}$ m^2/s for 60,000ppm KCl brine at 25°C (Harned & Nuttall, 1947; Lobo et al., 1998; He et al., 2015).

Figure 4-9 shows that the electrical tortuosity values for the Eagle Ford samples ranged from 2.1 to 5.8, the electrical tortuosity values for the Wolfcamp samples ranged from 2.1 to 4.2, the electrical tortuosity values for the Bakken samples ranged from 1.7 to 2.1, Utica sample had an electrical tortuosity value of 2.0 and the the electrical tortuosity values for the sandstone samples ranged from 1.5 to 3.6.

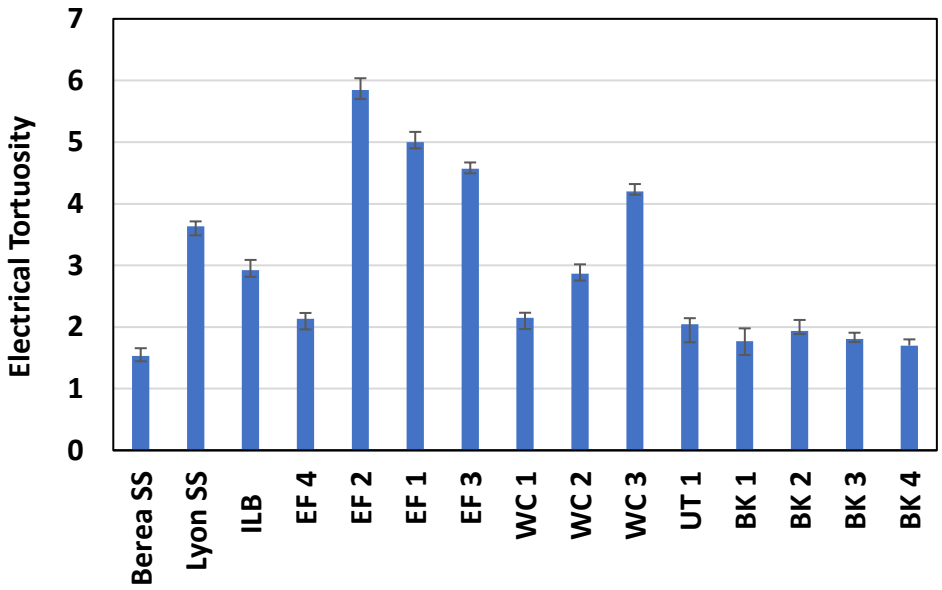

Figure 4-9. Electrical tortuosity values for the samples used in the study. Similar to the diffusional tortuosity measurements, the Berea sandstone sample shows the lowest electrical tortuosity, with the Eagle Ford samples showing the highest electrical tortuosity values.

4.3 Comparison Between Electrical and Diffusional Tortuosity

Figure 4-10 presents a comparison between the diffusional and electrical tortuosity. It is observed that the diffusional and electrical tortuosity have similar values for both the tight rock and sandstone samples. Therefore electrical current and fluid flow are subjected to the same flow path in porous media. This observation confirms the findings of (Clennell, 1997; Ghanbarian et al., 2013) based on their theoretical investigations.

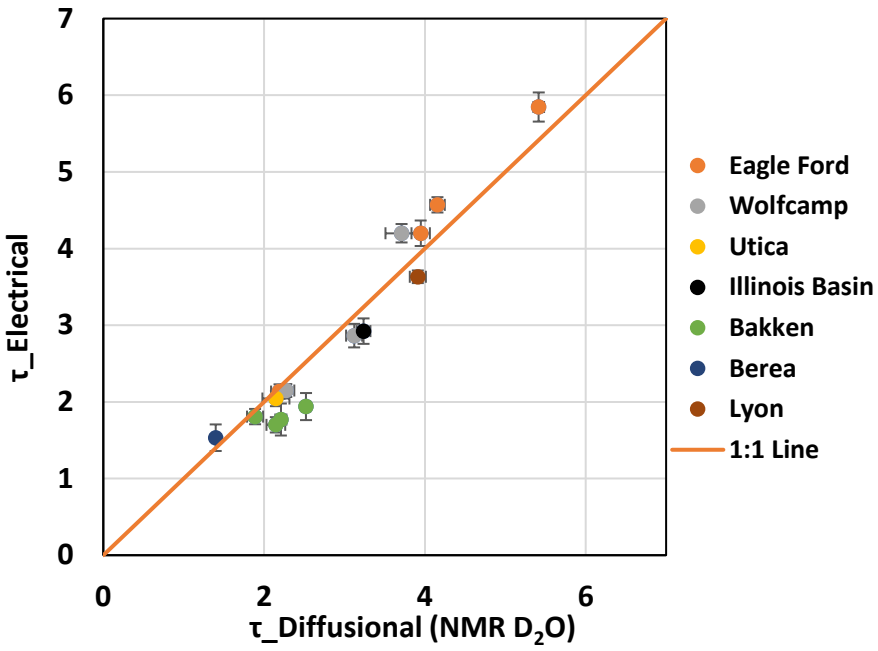

Figure 4-10. Comparison between diffusional and electrical tortuosity. Similar values of diffusional and electrical tortusoity are observed for the tight rock and sandstone samples used in this study.

4.4 Effective Porosity Computation

The knowledge of effective porosity is useful for the determination of electrical tortuosity directly from Eq. (2.11). The use of Eq. (2.11) is advantageous because resistivity formation factor measurements can be completed within minutes while the ionic diffusion measurements take weeks to complete.

To compute the effective porosity of the samples, I have taken advantage of the fact that two formulations can be used to compute electrical tortuosity. In section 4.2.2, the electrical tortuosity was computed using the ionic diffusion coefficients and it can also be computed using Eq. (2.11) Therefore equating Eq. (2.10) to Eq. (2.11), an expression for effective porosity is obtained.

$$Therefore, \emptyset_{eff} = \frac{\tau^2{}_{e\,(ionic\_diffusion)}}{F} \tag{4.7}$$

Figure 4-11 compares the effective porosity computed using Eq. (4.7) and the total porosity on brine saturated samples obtained from NMR measurements. It is observed that the effective and total porosity are almost equal for the sandstone samples and for the some of the tight rock samples from the Eagle Ford and Wolfcamp formations. However, in most of the tight rock samples, it was observed that the effective porosity is lower than the total porosity.

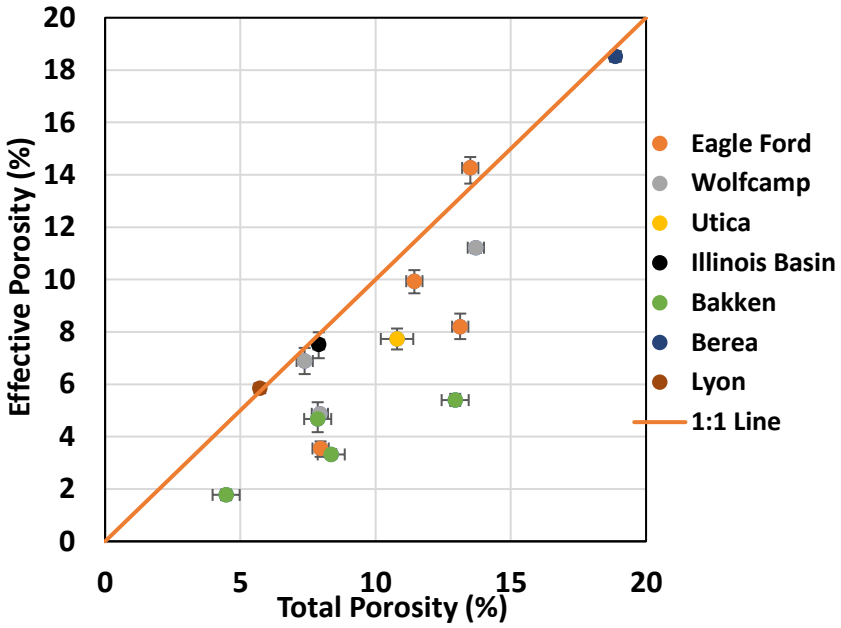

Figure 4-11. Comparison between effective porosity and total porosity. It is observed that the effective porosity is approximately 100% of the total porosity for the sandstone samples, while the tight rock samples have effective porosity ranging between 45 – 93% of the total porosity.

The difference between the NMR porosity obtained on saturated and dry samples could be interpreted as the effective porosity but as illustrated in **Figure 4-12**, it is seen that the effective porosity does not necessarily represent the difference between NMR saturated and dry porosity.

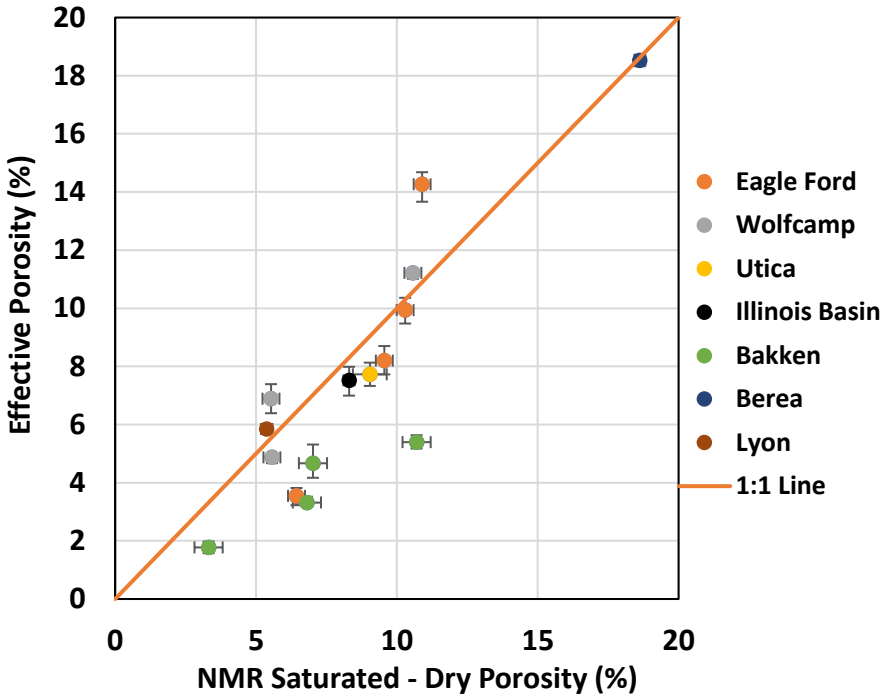

Figure 4-12. Comparison between effective porosity and the difference between NMR saturated and dry porosity. It is observed that the effective porosity does not equate to a difference between the saturated and dry NMR porosity.

Chapter 5 : Petrophysical Parameters Controlling Tortuosity and Effective Porosity

5.1 Factors Controlling Tortuosity

5.1.1 Tortuosity and Total Porosity

Figure 5-1 presents the cross plots between the measured tortuosities and the total porosity of the samples. The total porosity of the samples was obtained from NMR T_2 measurements after saturating the samples with 25,000 ppm KCl brine at 5,000 psi for 72 hours.

Unlike the observations made for sandstones and carbonates by Winsauer et al., (1952); Chen et al., (1977); Garrouch et al., (2001); Leger & Luquot (2021), There is no significant trend observed between the tortuosities of the tight rock samples and their total porosities.

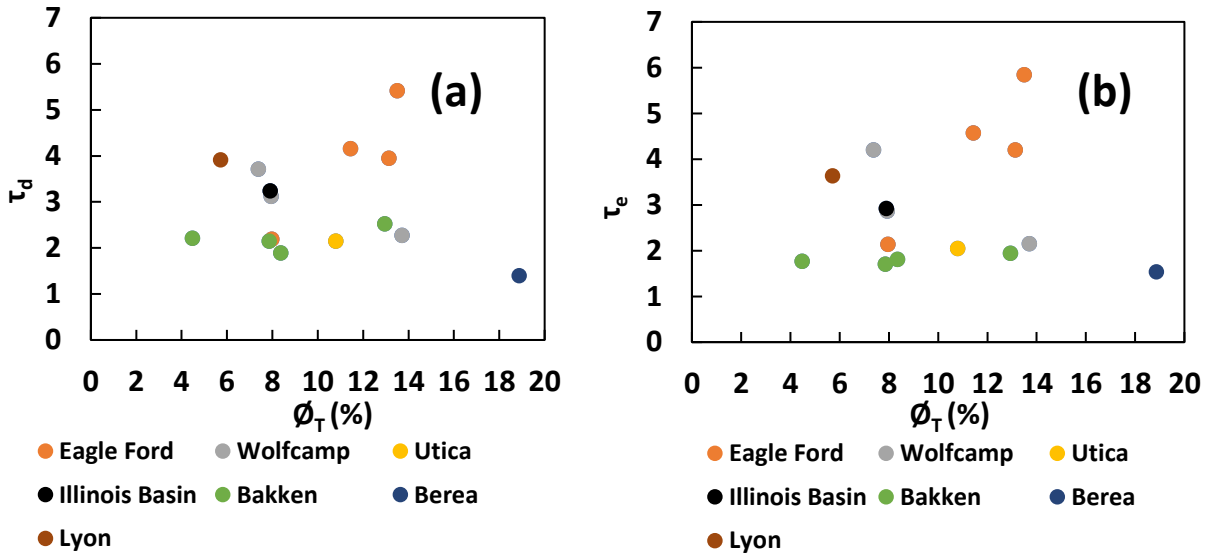

Figure 5-1. Relationships between diffusional tortuosity (a), electrical tortuosity (b) and total porosity. Both tortuosities do not exhibit a dependency on total porosity.

The diffusional tortusosity values obtained in this study were compared with literature values from previous studies (Chen et al. 1977; Dang et al. 2018, 2021; Fleury et al. 2009, 2010, 2016). It is observed that the diffusional tortuosity values published by Chen et al. (1977), Dang et al. (2018, 2021) and Fleury et al. (2009, 2010) are in the same range as values published in this present study. However, the diffusional tortuosity value of the Horn River shale by Fleury et al. (2016) appear to be larger than the diffusional tortuosity values of the samples used in this study. The analysis on **Figure 5-2** which includes the data from Chen et al. (1977), Dang et al. (2018, 2021), Fleury et al. (2009, 2010, 2016) and the data from this study shows that there is no correlation between diffusional tortuosity and total porosity.

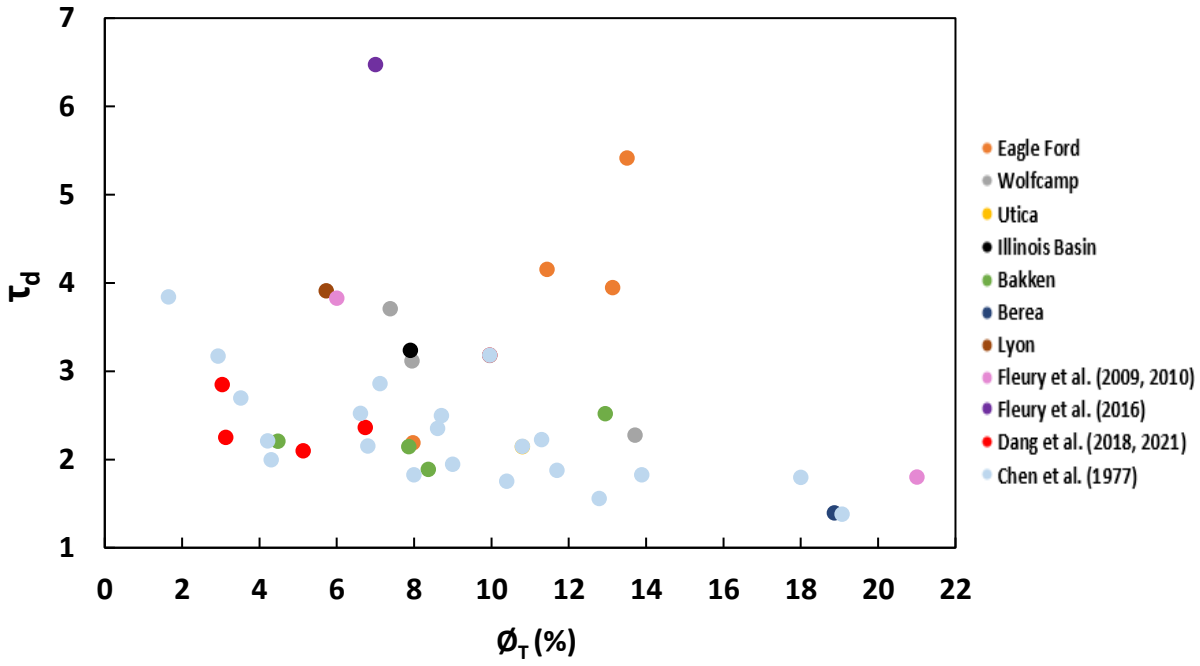

Figure 5-2. Relationship between diffusional tortuosity obtained in this study, Chen et al. (1977), Fleury et al. (2009, 2010, 2016) and Dang et al. (2018,2021) with total porosity. It is observed that the values obtained in this study show comparable values as a function of total porosity with previous studies in literature and there is no correlation between diffusional tortuosity and total porosity.

Similarly, it is observed that as a function of total porosity, the electrical tortuosity values of the the samples used in this study, show comparable results with literature values (Winsauer et al.,

1952; Garrouch et al., 2001; Leger & Luquot, 2021) at porosities greater than 10% while there are limited reported values in literature of electrical tortuosity values below 10%. A negative trend between electrical tortuosity and total porosity is observed in literature values from previous studies (Winsauer et al., 1952; Garrouch et al., 2001; Leger & Luquot, 2021) but the published values in this study do not show a correlation between electrical tortuosity and total porosity **(Figure 5-3)**.

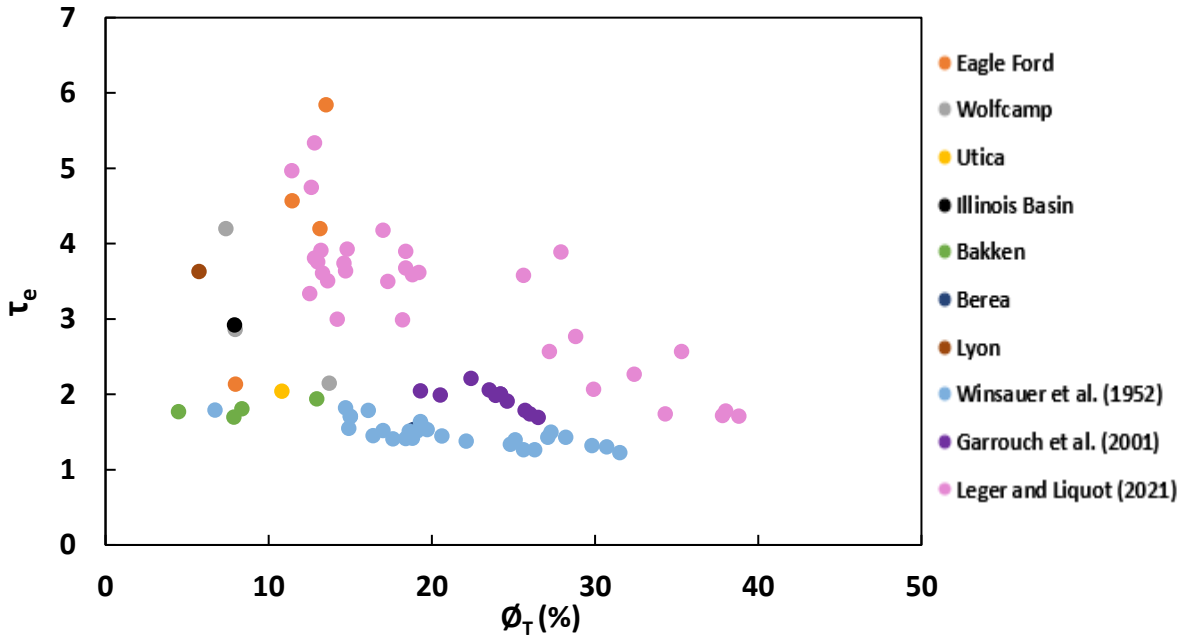

Figure 5-3. Relationship between electrical tortuosity obtained in this study, Winsauer et al. (1952), Garrouch et al. (2001) and Leger and Liquot (2021) with total porosity. It is observed that at porosity greater than 10%, the values obtained in this study show comparable values as a function of total porosity with previous studies in literature and the values obtained in this study do not show a correlation between electrical tortuosity and total porosity.

5.1.2 Tortuosity and Effective Porosity

Figure 5-4 illustrates the relationships between the measured tortuosities and the effective porosities of the samples. A positive linear relationship between the squared tortuosity and effective porosity is observed in the samples excluding the Berea sandstone.

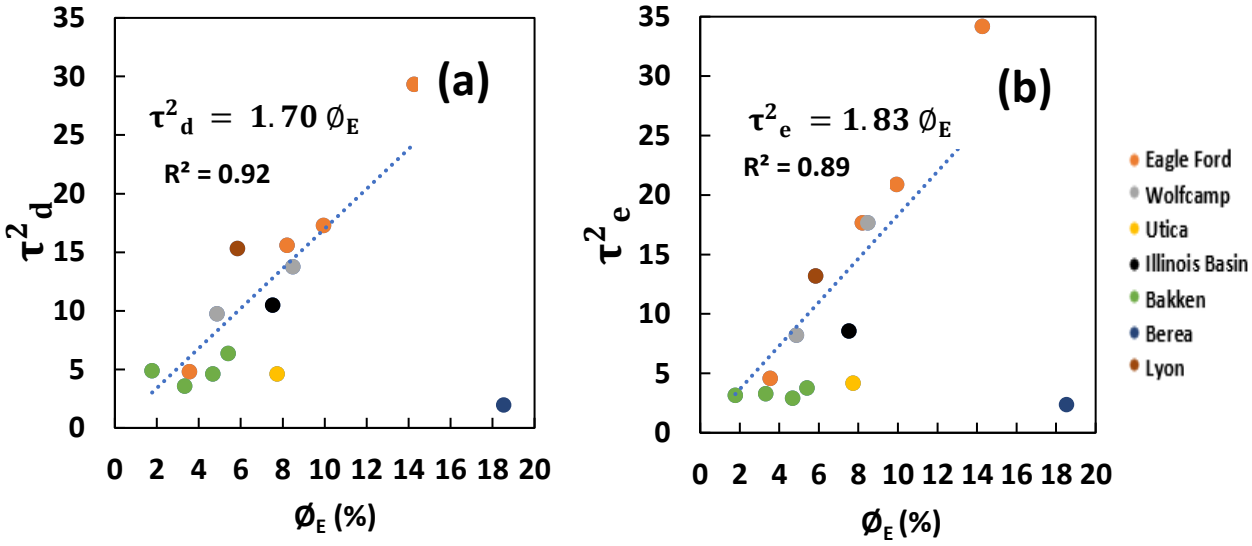

Figure 5-4. Relationships between diffusional tortuosity (a), electrical tortuosity (b) and effective porosity. The trendline represents only the tight rock samples used in this study.

5.1.3 Tortuosity and Mineralogy

Figures 5-5 and **5-6** present the relationship between the diffusional and electrical tortuosity respectively with the total clay, total carbonate, and quartz and feldspar content of the samples. The diffusional tortuosity data from this study was compared with values from Dang et al. (2018, 2021) and there were no observable trends between the diffusional tortuosity and the minerals considered.

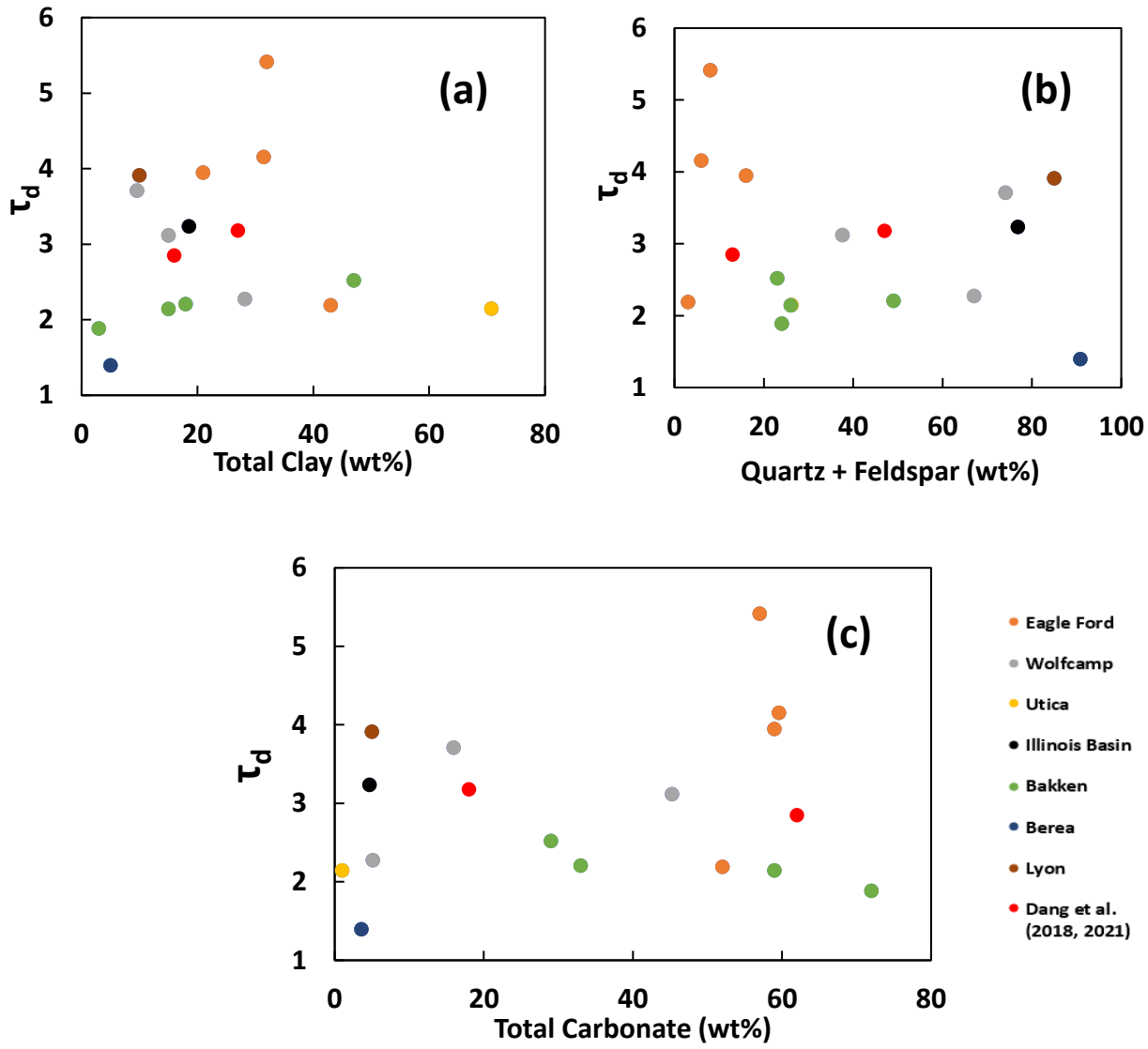

Figure 5-5. Relationship between diffusional tortuosity obtained in this study and from Dang et al. (2018, 2021) with total clay (a) quartz and feldspar (b) total carbonate (c). The diffusional tortuosity does not show a dependency on the minerals considered.

Similar to the observations made between the diffusional tortuosity and the minerals considered, there were no observable trends between the electrical tortuosity and the minerals considered. Therefore, this observation implies that mineralogy does not control tortuosity in tight rocks.

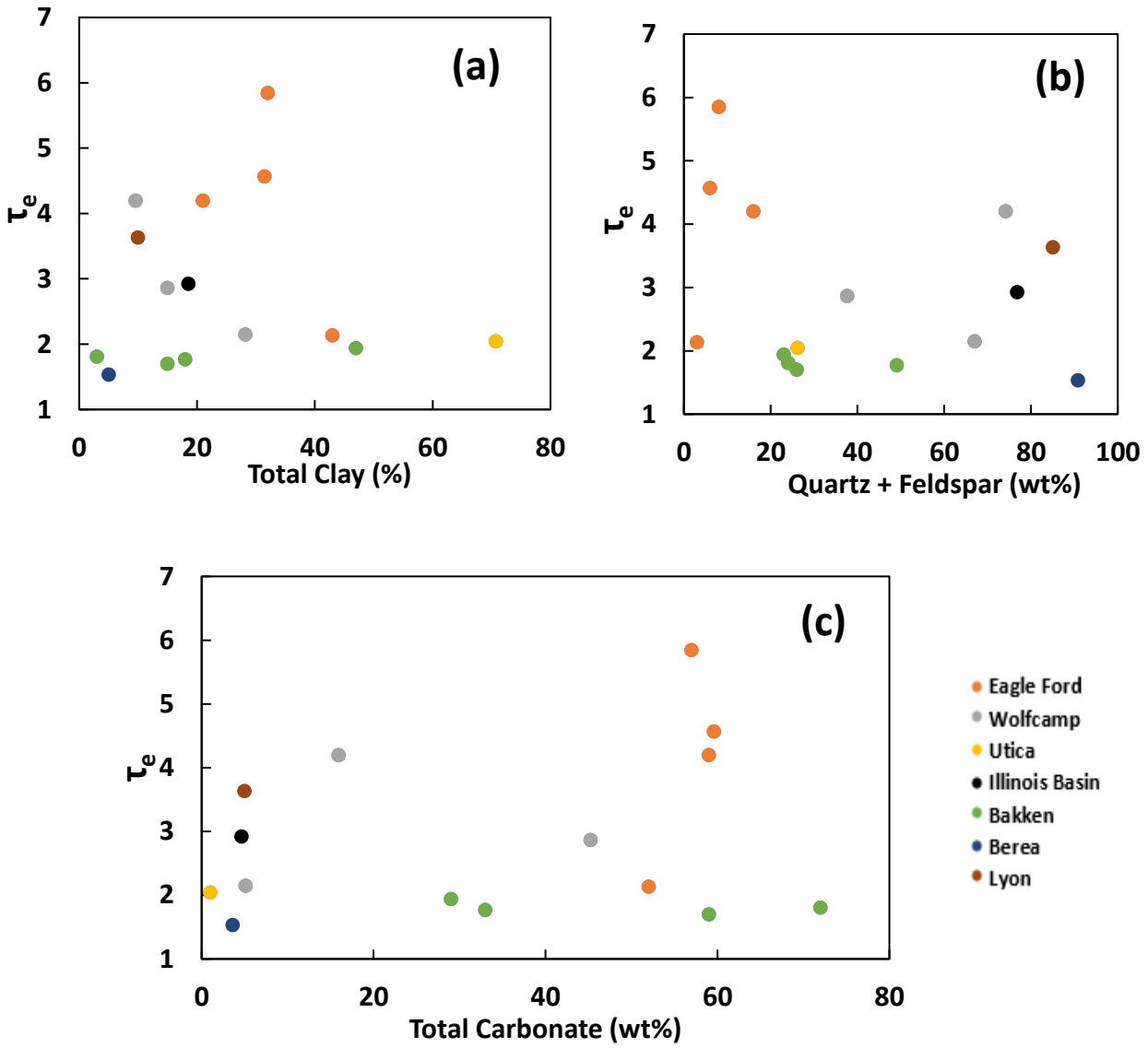

Figure 5-6. Relationship between electrical tortuosity and total clay (a) quartz and feldspar (b) total carbonate (c). The electrical tortuosity does not show a dependency on the minerals considered.

5.1.4 Tortuosity and TOC

Figures 5-7 and **5-8** present the relationship between the measured tortuosities and TOC. A positive linear trend between the measured tortuosities and TOC is observed for the tight rock samples. The significant correlation coefficients (> 0.7) implies that diffusional and electrical tortuosities are essentially controlled by the organic content.

Tortuosity is a measure of the complexity of the pore space (Clennell, 1997; Ghanbarian et al., 2013). Therefore, our previous observation imply that the presence of organic content increases the complexity of the flow paths.

Figure 5-7 shows that the large diffusional tortuosity for the Horn River shale sample by Fleury et al. (2016) is due to the fact that the sample has the largest TOC.

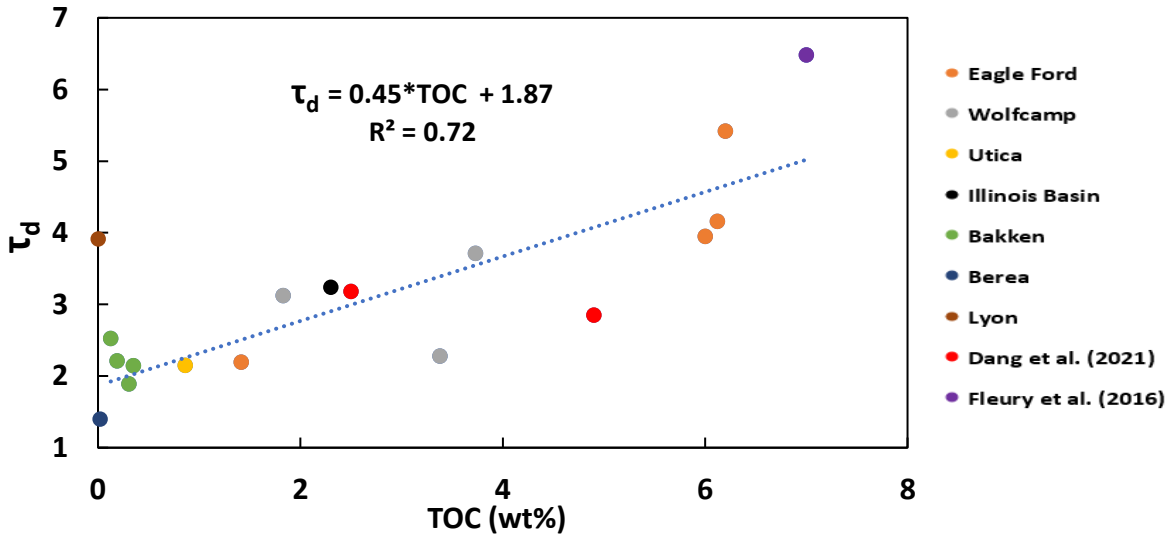

Figure 5-7. Relationship between diffusional tortuosity obtained in this study, Fleury et al. (2061) and Dang et al. (2021) with TOC. The trendline is representative of the tight rock samples. It is observed that Fleury (2016) Horn River shale and Dang et al. (2021) Wolfcamp sample and follow the same trend observed for the samples in this study.

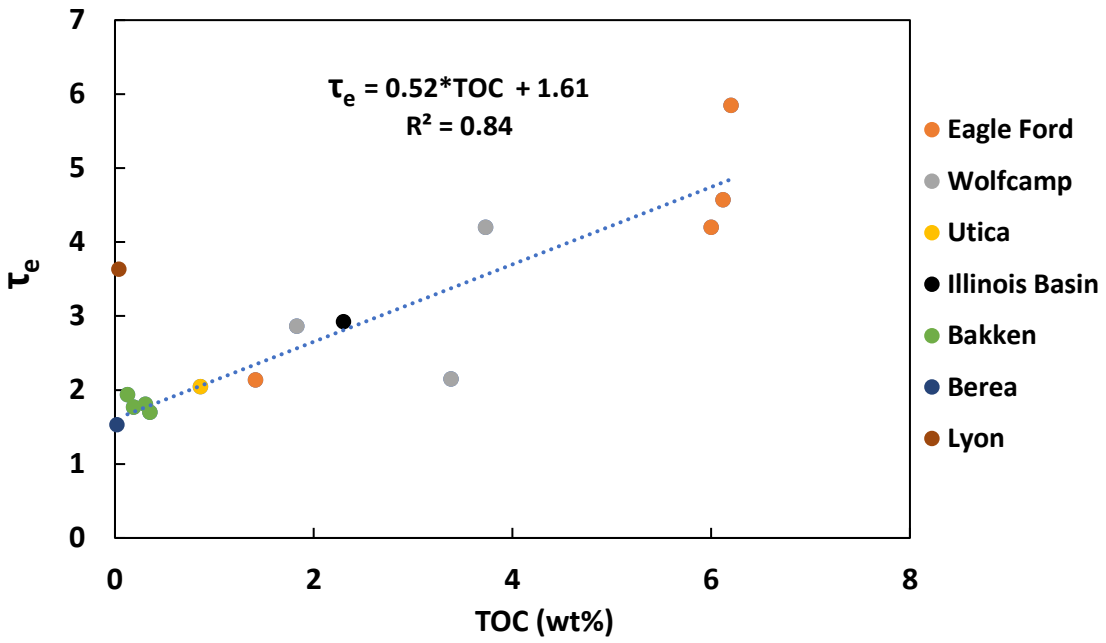

Figure 5-8. Relationship between electrical tortuosity and TOC. The trendline is representative of the tight rock samples. Similar to the diffusional tortuosity, a positive linear trend is observed.

5.1.5 Tortuosity and Pore Throat Size

Figures 5-9 illustrate the relationship between the measured tortuosities and average pore throat radius obtained from MICP measurements. There are two trends observed in the figures below. A weak negative linear trend between the measured tortuosities and average pore throat radius is observed in the tight rock samples and another negative trend between the measured tortuosities and average pore throat radius is observed in the sandstone samples. These observations can be

attributed to the fact that a reduction of the pore throat size leads to retardation of flow, thus increasing tortuosity.

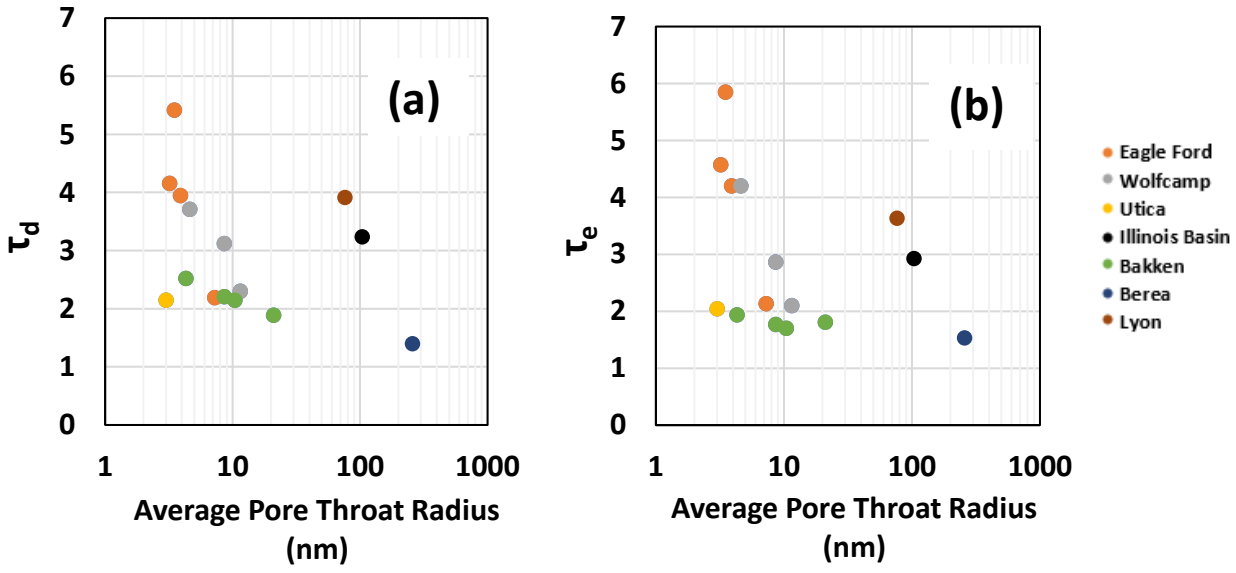

Figure 5-9. Relationships between diffusional tortuosity (a) and electrical tortuosity (b) with average pore throat radius determined from MICP measurements.

5.2 Factors Controlling Effective Porosity

5.2.1 Effective Porosity and Mineralogy

Figures 5-10 presents the relationship between the effective porosity and total clay, total carbonate, as well as quartz and feldspar content of the samples. No observable trends between effective porosity and the minerals considered was observed.

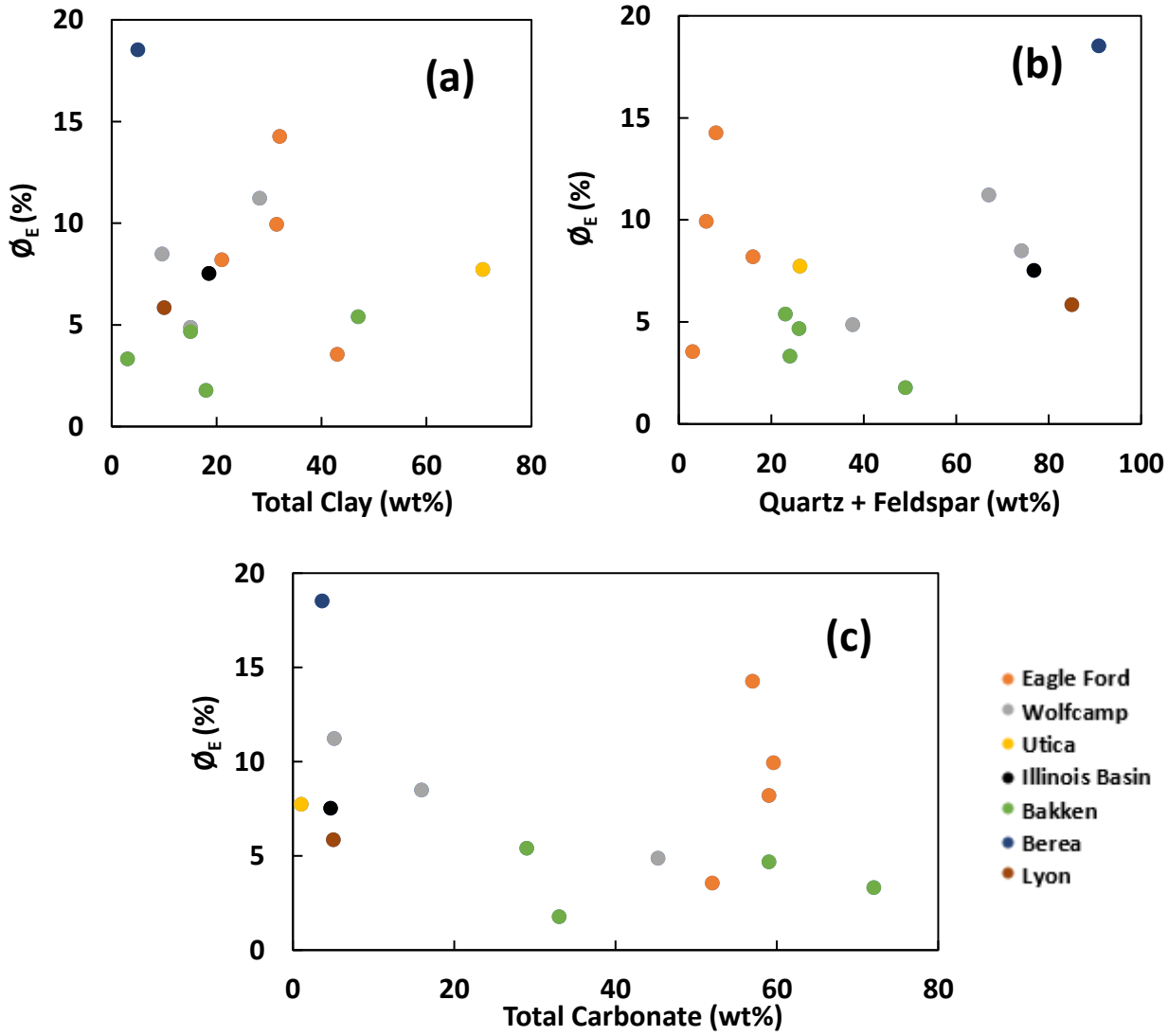

Figure 5-10. Relationship between effective porosity and total clay (a) quartz and feldspar (b) total carbonate (c). Effective porosity does not show a dependency on the minerals considered.

5.2.1 Effective Porosity and TOC

Figure 5-11 illustrates the relationship between effective porosity and TOC. A positive linear trend is observed for the tight rock samples.

Previous study have shown that a large fraction of the porosity of shale reservoirs is hosted in the organic matter (Loucks et al., 2009; Slatt & O'Brien, 2011; Curtis et al., 2012; Kuchinskiy, 2013; Haikuan et al., 2015). Therefore, the relationship between effective porosity and TOC can be explained the increase in the connectivity of the organic particles as TOC increases.

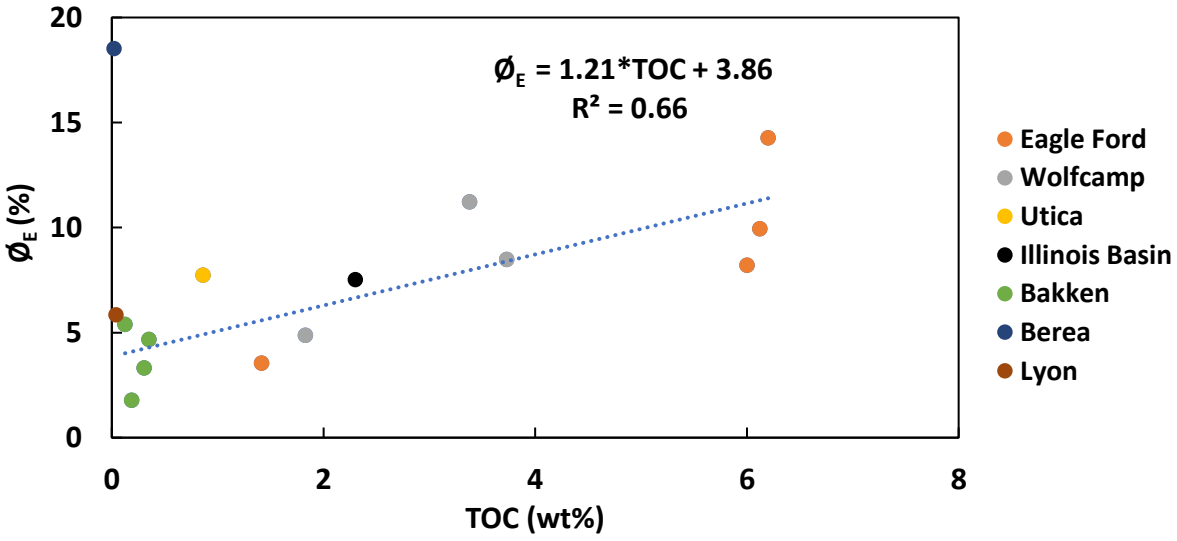

Figure 5-11. Relationship between effective porosity and TOC. The trendline is representative of the tight rock samples. A positive linear correlation is observed indicating that TOC controls effective porosity.

Chapter 6 : Conclusions

As part of this thesis, I have measured the diffusional tortuosity, electrical tortuosity and effective porosity on twelve tight rock samples from the Eagle Ford, Wolfcamp, Utica and Bakken formations and three sandstone samples from the Berea formation, Lyon formation and Illinois Basin. The analysis of the data collected shows that:

- The diffusional and electrical tortuosity have similar values for the tight rock and sandstone samples. This observation implies that the flow path for fluid and electrical current are the same in porous media. For the samples from the Eagle Ford and Wolfcamp formations, the tortuosities varied from 2.1 to 5.8, while the tortuosities of the samples from the Utica and Bakken formation varied from 1.8 to 2.5 and the tortuosities of the sandstone samples varied from 1.4 to 3.9.
- Tortuosity does not show a correlation with mineralogy. However, there is a strong positive linear relationship between tortuosity and TOC. Therefore, an increase in the organic matter content, increases the complexity of flow paths in the porous medium. This relationship between tortuosity and TOC implies that TOC can be used to predict tortuosity. A negative relationship was also observed between tortuosity and pore throat radius, which suggests that the reduction of the pore throat radius leads to retardation of flow, therby increasing tortuosity.
- The effective porosity computed in this present study ranged between 45 and 87% of the total porosity for samples from the Eagle Ford formation, while it ranged between 59 and 93% of the total porosity for samples from the Wolfcamp and Utica formation and it ranged between 40 and 59% of the total porosity for samples from the Bakken formation. It was

also observed that for the sandstone samples, the effective porosity was approximately equal to the total porosity.

- Effective porosity does not show a correlation with mineralogy. However, there is a positive linear relationship between effective porosity and TOC. The fact that most of the porosity in shales are hosted in organic matter, implies that an increase in the organic matter content increases the effective porosity.
- Effective porosity can be predicted from TOC and used in combination with the resistivity formation factor to determine the electrical tortuosity. The fact that resistivity formation factor measurements can be completed within minutes, while ionic diffusion measurements can take weeks to complete implies that the electrical tortuosity from resistivity formation factor would be faster to implement. This approach can also be applied to well log data where ionic diffusion coefficients cannot be measured.
- Tortuosity is an important parameteter that controls the injection gas penetration during EOR. The observation that diffusional and electrical tortuosity are similar implies that measurements of electrical tortuosity can be used to make decisions regarding the optimization of EOR design and strategy because electrical tortuosity can be obtained faster than diffusional tortuosity.

References

1. Ahmadi, M. M., Mohammadi, S., & Hayati, A. N. 2011. Analytical derivation of tortuosity and permeability of monosized spheres: A volume averaging approach. *Physical Review E*, **83** (2): 026312.

2. Almasoodi, M., & Reza, Z. 2019. Finite-Volume computations of shale tortuosity and permeability from 3D pore networks extracted from scanning electron tomographic images. Petrophysics - The *SPWLA Journal of Formation Evaluation and Reservoir Description*, **60** (03): 397–408. https://doi.org/10.30632/PJV60N3-2019a3

3. Amien, M. N., Pantouw, G. T., Juliust, H., & Eljabbar Latief, F. D. 2019. Geometric tortuosity analysis of porous medium using simple neurite tracer. *IOP Conference Series: Earth and Environmental Science*, **311** (1): 012041. https://doi.org/10.1088/1755-1315/311/1/012041

4. Archie, G. E. 1942. The electrical resistivity log as an aid in determining some reservoir characteristics. *Transactions of the AIME*, **146** (01): 54–62. SPE-942054-G. https://doi.org/10.2118/942054-G.

5. Azzam, M., & Dullien, F. 1977. Flow in tubes with periodic step changes in diameter: A numerical solution. *Chemical Engineering Science*, **32** (12): 1445–1455.

6. Backeberg, N. R., Iacoviello, F., Rittner, M., Mitchell, T. M., Jones, A. P., Day, R., Wheeler, J., Shearing, P. R., Vermeesch, P., & Striolo, A. 2017. Quantifying the anisotropy and tortuosity of permeable pathways in clay-rich mudstones using models based on x-ray tomography. *Scientific Reports*, **7** (1): 14838. https://doi.org/10.1038/s41598-017-14810-1.

7. Ballard, B. D. 2007. Quantitative mineralogy of reservoir rocks using fourier transform infrared spectroscopy. Presented at the SPE Annual Technical Conference and Exhibition, Anaheim, California, U.S.A., November 11–14, 2007. SPE-113023-STU. https://doi.org/10.2118/113023-STU.

8. Bauer, J. F., Krumbholz, M., Meier, S., & Tanner, D. C. 2017. Predictability of properties of a fractured geothermal reservoir: The opportunities and limitations of an outcrop analogue study. *Geothermal Energy*, **5** (1): 24. https://doi.org/10.1186/s40517-017-0081-0.

9. Baur, M. E., Garland, C. W., & Stockmayer, W. H. 1959. Diffusion coefficients of H_2O-D_2O mixtures. *Journal of the American Chemical Society*, **81** (12): 3147–3148. https://doi.org/10.1021/ja01521a058.

10. Beeckman, J. 1990. Mathematical description of heterogeneous materials. *Chemical Engineering Science*, **45** (8): 2603–2610.

11. Bernabe, Y. 1991. Pore geometry and pressure dependence of the transport properties in sandstones. *Geophysics*, **56** (4): 436–446.

12. Bezzar, A., & Ghomari, F. 2013. Monitoring of pollutant diffusion into clay liners by electrical methods. *Transport in Porous Media*, **97** (2): 147–159. https://doi.org/10.1007/s11242-012-0115-9

13. Bo-Ming, Y., & Jian-Hua, L. 2004. A geometry model for tortuosity of flow path in porous media. *Chinese Physics Letters*, **21** (8): 1569.

14. Brown, S. R. 1989. Transport of fluid and electric current through a single fracture. *Journal of Geophysical Research: Solid Earth*, **94** (B7): 9429–9438.

15. Bustin, A. M. M., Bustin, R. M., & Cui, X. 2008. Importance of fabric on the production of gas shales. Unconventional Gas Conference, Keystone, Colorado, February 10–12, 2008. SPE-114167-MS. https://doi.org/10.2118/114167-MS.

16. Cai, J., Wei, W., Hu, X., & Wood, D. A. 2017. Electrical conductivity models in saturated porous media: a review. *Earth-Science Reviews*, **171**. 419–433. https://doi.org/10.1016/j.earscirev.2017.06.013

17. Carman, P. C. 1937. Fluid flow through granular beds. *Chemical Engineering Research and Design*, **75**: S32–S48. https://doi.org/10.1016/S0263-8762(97)80003-2

18. Carman, P. Crosbie. (1956). *Flow of gases through porous media.* Academic Press.

19. Chen, L. L., Katz, D. L., & Tek, M. R. 1977. Binary gas diffusion of methane-nitrogen through porous solids. *AIChE Journal*, **23** (3): 336–341.

20. Chen, M., Kang, Y., Zhang, T., You, L., Li, X., Chen, Z., Wu, K., & Yang, B. 2018. Methane diffusion in shales with multiple pore sizes at supercritical conditions. *Chemical Engineering Journal*, **334**: 1455–1465.

21. Clennell, M. B. 1997. Tortuosity: A guide through the maze. *Geological Society, London, Special Publications*, **122** (1): 299. https://doi.org/10.1144/GSL.SP.1997.122.01.18

22. Coleman, S., & Vassilicos, J. 2008. Transport properties of saturated and unsaturated porous fractal materials. *Physical Review Letters*, **100** (3): 035504.

23. Coussy, O. 1995. *Mechanics of porous continua*. Wiley.

24. Crank, J. 1975. *The mathematics of diffusion / by J. Crank*. Clarendon Press.

25. Cronin, M., Emami-Meybodi, H., & Johns, R. T. 2019. Unified theory of ultimate hydrocarbon recovery for primary and cyclic injection processes in ultra-tight reservoirs. *Scientific Reports*, **9** (1): 10706–10706. PubMed. https://doi.org/10.1038/s41598-019-47099-3.

26. Curtis, M. E., Ambrose, J., Sondergeld, H., & Rai, C. S. 2011a. Investigating the microstructure of gas shales by fib/sem tomography & stem imaging. In Presentation given at the Oklahoma Geological Survey workshop, Vol. 21, Norman, Oklahoma.

27. Curtis, M. E., Ambrose, R. J., Sondergeld, C. H., & Rai, C. S. 2011b. Investigation of the relationship between organic porosity and thermal maturity in the Marcellus shale. Presented at the North American Unconventional Gas Conference and Exhibition, The Woodlands, Texas, USA, June 14–16, 2011. SPE-144370-MS. https://doi.org/10.2118/144370-MS.

28. Curtis, M. E., Cardott, B. J., Sondergeld, C. H., & Rai, C. S. 2012. Development of organic porosity in the Woodford shale with increasing thermal maturity. *International Journal of Coal Geology*, **103**: 26–31.

29. Dang, S., Mukherjee, S., Sondergeld, C., & Rai, C. 2021. Measurement of effective tortuosity in unconventional tight rock using nuclear magnetic resonance. In Unconventional Resources Technology Conference, 26–28 July 2021 (pp. 1476-1489). URTEC-2021-5118-MS. https://doi.org/10.15530/urtec-2021-5118

30. Dang, S. T., Sondergeld, C. H., Rai, C. S., Tinni, A. O., & Drenzek, N. 2018. A first step in evaluating the role of diffusion in EOR in tight shale formations. SCA-2018.

31. Davudov, D., G Moghanloo, R., & Lan, Y. 2018. Evaluation of accessible porosity using mercury injection capillary pressure data in shale samples. *Energy & Fuels,* **32**. https://doi.org/10.1021/acs.energyfuels.7b03930.

32. Do, D. D., & Do, H. D. 2003. Pore characterization of carbonaceous materials by DFT and GCMC Simulations: a review. *Adsorption Science & Technology*, **21** (5): 389–423. https://doi.org/10.1260/026361703769645753

33. Du Plessis, J. P., & Masliyah, J. H. 1991. Flow through isotropic granular porous media. *Transport in Porous Media*, **6** (3): 207–221.

34. Duda, A., Koza, Z., & Matyka, M. 2011. Hydraulic tortuosity in arbitrary porous media flow. *Physical Review E*, **84** (3): 036319. https://doi.org/10.1103/PhysRevE.84.036319

35. Dullien, F. A. L. 1992. 3—Single-Phase transport phenomena in porous media. In F. A. L. Dullien (Ed.), *Porous Media (Second Edition)* (pp. 237–317). Academic Press. https://doi.org/10.1016/B978-0-12-223651-8.50009-2

36. Energy Information Administration 2019. Technically Recoverable Shale Oil and Shale Gas Resources: An assessment of 137 Shale Formations in 41 countries outside the United States.

37. Epstein, N. 1989. On tortuosity and the tortuosity factor in flow and diffusion through porous media. *Chemical Engineering Science*, **44** (3): 777–779. https://doi.org/10.1016/0009-2509(89)85053-5

38. Er, C., Li, Y., Zhao, J., Wang, R., Bai, Z., & Han, Q. 2016. Pore formation and occurrence in the organic-rich shales of the Triassic Chang-7 Member, Yanchang Formation,

Ordos Basin, China. *Journal of Natural Gas Geoscience*, **1** (6): 435–444. https://doi.org/10.1016/j.jnggs.2016.11.013.

39. Eslinger, E., & Pevear, D. 1985. *Clay minerals for petroleum geologists and engineers*. SEPM Society for Sedimentary Geology.

40. Ezekwe, N. 2010. *Petroleum Reservoir Engineering Practice*. Pearson Education.

41. Fatt, I. 1956. The network model of porous media. *Transactions of the AIME*, **207** (01), 144–181. SPE-574-G. https://doi.org/10.2118/574-G.

42. Fetter, C. W. 1988. *Applied Hydrogeology* (2nd ed., p. 592). New York: Macmillan Publishing Company.

43. Fetter, C. W. 1993. *Contaminant Hydrogeology* (p. 458). New York: Macmillan Publishing Company.

44. Fleury, M., P. Berne, and P. Bachaud 2009. Diffusion of dissolved CO2 in caprock. *Energy Procedia*, **1** (1)*: 3461–3468*. https://doi.org/10.1016/j.egypro.2009.02.137.

45. Fleury, M., Gautier, S., Gland, N., Boulin, P., Norden, B., & Schmidt-Hattenberger, C. 2010. Petrophysical measurements for CO2 storage: Application to the Ketzin site. In International Symposium of the Society of Core Analysts, Halifax, Nova Scotia, Canada (pp. 4-7).

46. Fleury, M., and M. Romero-Sarmiento 2016, Characterization of shales using T1–T2 NMR maps. *Journal of Petroleum Science and Engineering*, **137**: *55–62.* https://doi.org/10.1016/j.petrol.2015.11.006.

47. Fleury, M., & Brosse, E. 2018. Transport in tight rocks. In *Geological Carbon Storage (eds S. Vialle, J. Ajo-Franklin and J.W. Carey), 31–43.* https://doi.org/10.1002/9781119118657.ch2.

48. Fleury, M., Chevalier, T., Berthe, G., Dridi, W., & Adadji, M. 2020. Water diffusion measurements in cement paste, mortar and concrete using a fast NMR based technique. *Construction and Building Materials*, ***259***: 119843. https://doi.org/10.1016/j.conbuildmat.2020.119843.

49. Fleury, M., Efnik, M., & Kalam, M. 2004. Evaluation of water saturation from resistivity in a carbonate field. From laboratory to logs. In *Proceedings of International Symposium of the Society of Core Analysts, Abu Dhabi, UAE,* pp. 5-9. 2004.

50. Fredrich, J. T., Lindquist, W. B., Noble, D. R., & O'Connor, R. M. 1999. Development, implementation, and experimental validation of the lattice Boltzmann method for modeling three-dimensional complex flows (No. SAND99-0369). Sandia National Lab.(SNL-NM), Albuquerque, NM (United States); Sandia National Lab.(SNL-CA), Livermore, CA (United States).

51. Fu, J., Thomas, H. R., & Li, C. 2021. Tortuosity of porous media: Image analysis and physical simulation. *Earth-Science Reviews*, **212**: 103439. https://doi.org/10.1016/j.earscirev.2020.103439.

52. Garcia, A. P., Han, Y., & Heidari, Z. 2018. Integrated workflow to estimate permeability through quantification of rock fabric using joint interpretation of nuclear magnetic resonance and electric measurements. *Petrophysics-The SPWLA Journal of*

Formation Evaluation and Reservoir Description, **59** (05): 672-693. https://doi.org/10.30632/PJV59N5-2018a7.

53. Garrouch, Ali. A., Ali, L., & Qasem, F. 2001. Using diffusion and electrical measurements to assess tortuosity of porous media. *Industrial & Engineering Chemistry Research*, **40** (20): 4363–4369. https://doi.org/10.1021/ie010070u.

54. Garum, M., Glover, P. P., Hassanpour, A., & Lorinczi, P. P. 2019. Fluid flow and microstructural properties of gas shales. In 81st EAGE Conference and Exhibition 2019 (Vol. 2019, No. 1, pp. 1-5). https://doi.org/10.3997/2214-4609.201901110.

55. Georgali, B., & Tsakiridis, P. 2005. Microstructure of fire-damaged concrete. A case study. *Cement and Concrete Composites*, **27** (2): 255–259.

56. Ghanbarian, B., Hunt, A. G., Ewing, R. P., & Sahimi, M. 2013. Tortuosity in porous media: A critical review. *Soil Science Society of America Journal*, **77** (5): 1461–1477. https://doi.org/10.2136/sssaj2012.0435.

57. Gong, L., Nie, L., & Xu, Y. 2020. Geometrical and Topological Analysis of Pore Space in Sandstones Based on X-ray Computed Tomography. *Energies*, **13** (15). https://doi.org/10.3390/en13153774.

58. Gonzalez, A., Heidari, Z., & Lopez, O. 2021. Electrical, diffusional, and hydraulic tortuosity anisotropy quantification using 3D CT-scan image data. Presented at the SPE Annual Technical Conference and Exhibition, Dubai, UAE, September 21–23, 2021. SPE-206109-MS. https://doi.org/10.2118/206109-MS.

59. Haikuan, N., Jinchuan, Z., & Shengling, J. 2015. Types and characteristics of the lower Silurian shale gas reservoirs in and around the Sichuan Basin. *Acta Geologica Sinica-English Edition*, **89** (6): 1973–1985.

60. Harned, H. S., & Nuttall, R. L. 1947. The diffusion coefficient of potassium chloride in dilute aqueous solution. *Journal of the American Chemical Society*, **69** (4): 736–740. https://doi.org/10.1021/ja01196a002.

61. Hatch, J., Jacobson, R., Mastalerz, M., Andrews, W., Weisenfluh, J., Affolter, R., & Gunther, G. 2002. *Resource assessment of the Springfield, Herrin, Danville, and Baker coals in the Illinois Basin (No. 072–02)*. https://doi.org/10.3133/fs07202.

62. He, M., Zhang, S., Zhang, Y., & Peng, S. 2015. Development of measuring diffusion coefficients by digital holographic interferometry in transparent liquid mixtures. *Optics Express*, **23** (9): 10884–10899.

63. Hoffman, B. T., & Rutledge, J. M. 2019. Mechanisms for Huff-n-Puff cyclic gas injection into unconventional reservoirs. In SPE Oklahoma City Oil and Gas Symposium, Oklahoma City, Oklahoma, USA, April 9–10, 2019. SPE-195223-MS. https://doi.org/10.2118/195223-MS.

64. Hu, Q., Ewing, R. P., & Dultz, S. 2012. Low pore connectivity in natural rock. *Journal of Contaminant Hydrology*, **133**: 76–83.

65. Hu, Q., Gao, X., Gao, Z., Ewing, R., Dultz, S., & Kaufmann, J. 2014. Pore accessibility and connectivity of mineral and kerogen phases for shales. In Unconventional Resources Technology Conference, Denver, Colorado, 25-27 August 2014. pp. 1188-1204. URTEC-1922943-MS. https://doi.org/10.15530/urtec-2014-1922943.

66. Jamialahmadi, M., Emadi, M., & Müller-Steinhagen, H. 2006. Diffusion coefficients of methane in liquid hydrocarbons at high pressure and temperature. *Journal of Petroleum Science and Engineering*, **53** (1–2): 47–60.

67. Janiga, D., Czarnota, R., Kuk, E., Stopa, J., & Wojnarowski, P. 2020. Measurement of Oil-CO2 diffusion coefficient using pulse-echo method for pressure-volume decay approach under reservoir conditions. *Journal of Petroleum Science and Engineering*, **185***:* 106636. https://doi.org/10.1016/j.petrol.2019.106636.

68. Jin, G., Patzek, T. W., & Silin, D. B. 2004. Direct prediction of the absolute permeability of unconsolidated and consolidated reservoir rock. Presented at the SPE Annual Technical Conference and Exhibition, Houston, Texas, September 26–29, 2004. SPE-90084-MS. https://doi.org/10.2118/90084-MS.

69. Kadkhodaie, A., & Rezaee, R. 2016. A new correlation for water saturation calculation in gas shale reservoirs based on compensation of kerogen-clay conductivity. *Journal of Petroleum Science and Engineering*, **146**: 932–939.

70. Keehm, Y. 2003. *Computational rock physics: Transport properties in porous media and applications*. Stanford University.

71. Klaver, J., Hemes, S., Houben, M., Desbois, G., Radi, Z., & Urai, J. 2015. The connectivity of pore space in mudstones: Insights from high-pressure Wood's metal injection, BIB-SEM imaging, and mercury intrusion porosimetry. *Geofluids*, **15** (4), 577–591.

72. Klinkenberg, L. J. 1951. Analogy between diffusion and electrical conductivity in porous rocks. *GSA Bulletin*, **62** (6), 559–564. https://doi.org/10.1130/0016-7606(1951)62[559:ABDAEC]2.0.CO;2.

73. Kozeny, J. 1927. Uber Kapillare Leitung der Wasser in Boden. *Royal Academy of Science, Vienna, Proc. Class I*, **136**: 271–306.

74. Kuchinskiy, V. 2013. Organic porosity study: Porosity development within organic matter of the lower Silurian and Ordovician source rocks of the Poland shale gas trend. In *AAPG Annual Meeting. Search and Discovery Article* (Vol. 10522).

75. Kuila, U., & Prasad, M. 2013. Specific surface area and pore-size distribution in clays and shales. *Geophysical Prospecting*, **61** (2): 341–362. https://doi.org/10.1111/1365-2478.12028

76. Labani, M., & Rezaee, R. 2015. Petrophysical evaluation of gas shale reservoirs. *Fundamentals of Gas Shale Reservoirs*, 117–137. https://doi.org/10.1002/9781119039228.ch6

77. Lanfrey, P.-Y., Kuzeljevic, Z., & Dudukovic, M. 2010. Tortuosity model for fixed beds randomly packed with identical particles. *Chemical Engineering Science*, **65** (5): 1891–1896.

78. Leger, M., & Luquot, L. 2021. Importance of Microstructure in Carbonate Rocks: Laboratory and 3D-Imaging Petrophysical Characterization. *Applied Sciences*, **11** (9): 3784.

79. Li, J.-H., & Yu, B.-M. 2011. Tortuosity of flow paths through a Sierpinski carpet. *Chinese Physics Letters*, **28** (3): 034701.

80. Li, Z., Yuan, L., Sun, G., Lv, J., & Zhang, Y. 2021. Experimental determination of CO_2 diffusion coefficient in a brine-saturated core simulating reservoir condition. *Energies*, **14** (3): 540.

81. Lobo, V. M., Ribeiro, A. C., & Verissimo, L. M. 1998. Diffusion coefficients in aqueous solutions of potassium chloride at high and low concentrations. *Journal of Molecular Liquids*, **78** (1–2): 139–149.

82. Loucks, R. G., Reed, R. M., Ruppel, S. C., & Jarvie, D. M. 2009. Morphology, genesis, and distribution of nanometer-scale pores in siliceous mudstones of the Mississippian Barnett Shale. *Journal of Sedimentary Research*, **79** (12): 848–861.

83. Loucks, R. G., Ruppel, S., Reed, R. M., Hammes, U., & Zahm, C. 2011. Origin and classification of pores in mudstones from shale-gas systems. *Search and Discovery Article*, *40855*, 1–32.

84. Ma, B., Hu, Q., Yang, S., Yin, N., Qiao, H., Zhang, T., & Meng, M. 2020. Multiple approaches to quantifying the effective porosity of lacustrine shale oil reservoirs in Bohai Bay Basin, East China. *Geofluids*, *2020*, 8856620. https://doi.org/10.1155/2020/8856620.

85. Marsily, G. de. 1986. *Quantitative hydrogeology: Groundwater hydrology for engineers*. Academic Press.

86. Martys, N., Torquato, S., & Bentz, D. 1994. Universal scaling of fluid permeability for sphere packings. *Physical Review. E, Statistical Physics, Plasmas, Fluids, and Related Interdisciplinary Topics*, **50**: 403–408. https://doi.org/10.1103/PhysRevE.50.403

87. Maxwell, J. C. 1873. *A treatise on electricity and magnetism* (Vol. 1). Clarendon Press.

88. McPhee, C., Reed, J., & Zubizarreta, I. 2015. *Core analysis: A best practice guide*. Elsevier.

89. Meng, W., Xia, Y., Chen, Y., & Pu, X. 2018. Measuring the mutual diffusion coefficient of heavy water in normal water using a double liquid-core cylindrical lens. *Scientific Reports*, **8** (1). 12610. https://doi.org/10.1038/s41598-018-30650-z.

90. Mills, R. 1973. Self-diffusion in normal and heavy water in the range 1-45.deg. *The Journal of Physical Chemistry*, **77** (5): 685–688. https://doi.org/10.1021/j100624a025.

91. Mukherjee, S., Dang, S. T., Rai, C. S., & Sondergeld, C. H. 2020. Measurement of oil-gas diffusivity at reservoir conditions for Huff-n-Puff EOR in shales. Presented at the SPE Improved Oil Recovery Conference, Virtual, August 31–September 4, 2020. SPE-200306-MS. https://doi.org/10.2118/200306-MS.

92. Munroe, P. R. 2009. The application of focused ion beam microscopy in the material sciences. *Materials Characterization*, **60** (1): 2–13.

93. Nelson, P. H. 2009. Pore-throat sizes in sandstones, tight sandstones, and shales. *AAPG Bulletin*, **93** (3): 329–340. https://doi.org/10.1306/10240808059.

94. Nguyen, N. T. B., Dang, C. T. Q., Chen, Z., & Nghiem, L. X. 2015. Optimization of hydraulic fracturing design with future EOR considerations in shale oil reservoirs. Presented at the EUROPEC 2015, Madrid, Spain, June 1–4, 2015. SPE-174307-MS. https://doi.org/10.2118/174307-MS.

95. Odiachi, J., Cruz, F., & Tinni, A. 2021. Experimental study of hydrocarbon vaporization for EOR applications. Paper presented at the SPE/AAPG/SEG Unconventional Resources Technology Conference, Houston, Texas, USA, July 2021. URTEC-2021-5674-MS. https://doi.org/10.15530/urtec-2021-5674.

96. Odiachi, J., Tinni, A., Sondergeld, C. H., & Rai, C. S. 2021. Determination of pore fluid salinity in tight rocks without fluid extraction. Paper presented at the SPE/AAPG/SEG Unconventional Resources Technology Conference, Houston, Texas, USA, July 2021. URTEC-2021-5679-MS. https://doi.org/10.15530/urtec-2021-5679.

97. Petersen, E. E. 1958. Diffusion in a pore of varying cross section. *A. I. Ch. E. Journal*, *Vol: 4*. https://doi.org/10.1002/aic.690040322.

98. Peveraro, R., & Thomas, E. C. 2010. Effective Porosity: A defensible definition for shaly sands. Paper presented at the SPWLA 51st Annual Logging Symposium, Perth, Australia, June 2010. SPWLA-2010-97677.

99. Piller, M., Schena, G., Nolich, M., Favretto, S., Radaelli, F., & Rossi, E. 2009. Analysis of hydraulic permeability in porous media: From high resolution X-ray tomography to direct numerical simulation. *Transport in Porous Media*, **80** (1): 57–78.

100. Qinhong, H., ZHANG, Y., Xianghao, M., Zheng, L., Zhonghuai, X., & Maowen, L. 2017. Characterization of micro-nano pore networks in shale oil reservoirs of Paleogene Shahejie Formation in Dongying Sag of Bohai Bay Basin, East China. *Petroleum Exploration and Development*, **44** (5): 720–730.

101. Riazi, M. R. 1996. A new method for experimental measurement of diffusion coefficients in reservoir fluids. *Journal of Petroleum Science and Engineering*, **14** (3–4): 235–250.

102. Roque, W. L. and Siebert, D. N. 2020. Reservoir rock tortuosity estimates based on geodesic reconstruction and fluid velocity field techniques. Presented at the SPE Europec, Virtual, December 1–3, 2020. SPE-200535-MS. https://doi.org/10.2118/200535-MS.

103. Salama, A., Amin, M. F. E., Kumar, K., & Sun, S. 2017. Flow and transport in tight and shale formations: A review. *Geofluids, 2017*. 1-21. http://dx.doi.org/10.1155/2017/4251209.

104. Saomoto, H., & Katagiri, J. 2015. Direct comparison of hydraulic tortuosity and electric tortuosity based on finite element analysis. *Theoretical and Applied Mechanics Letters*, **5** (5): 177–180. https://doi.org/10.1016/j.taml.2015.07.001.

105. Seaton, N., & Walton, J. 1989. A new analysis method for the determination of the pore size distribution of porous carbons from nitrogen adsorption measurements. *Carbon*, **27** (6): 853–861.

106. Sheng, J. J. 2015. Increase liquid oil production by huff-n-puff of produced gas in shale gas condensate reservoirs. *Journal of Unconventional Oil and Gas Resources*, **11:** 19–26. https://doi.org/10.1016/j.juogr.2015.04.004.

107. Shi, Z., Wen, B., Hesse, M., Tsotsis, T., & Jessen, K. 2018. Measurement and modeling of CO2 mass transfer in brine at reservoir conditions. *Advances in Water Resources*, **113**: 100–111.

108. Slatt, R. M., & O'Brien, N. R. 2011. Pore types in the Barnett and Woodford gas shales: Contribution to understanding gas storage and migration pathways in fine-grained rocks. *AAPG Bulletin*, **95** (12): 2017–2030.

109. Sondergeld, C. H., & Rai, C. S. 1993. A new exploration tool: Quantitative core characterization. In *Experimental Techniques in Mineral and Rock Physics* (pp. 249–268). Springer.

110. Spanne, P., Thovert, J., Jacquin, C., Lindquist, W., Jones, K., & Adler, P. 1994. Synchrotron computed microtomography of porous media: Topology and transports. *Physical Review Letters*, **73** (14): 2001.

111. Spooner, P. 2014. Lifting the fog of confusion surrounding clay and shale in petrophysics. SPWLA 55th Annual Logging Symposium Abu Dhabi, United Arab Emirates. May 2014. SPWLA-2014-VV.

112. Srisutthiyakorn, N., & Mavko, G. 2016. Hydraulic Tortuosity: From artificial packs to natural rocks. In *SEG Technical Program Expanded Abstracts 2016* (Vol. 1–0, pp. 3133–3137). https://doi.org/10.1190/segam2016-13966753.1.

113. Stutzman, P. 2004. Scanning electron microscopy imaging of hydraulic cement microstructure. *Cement and Concrete Composites*, **26** (8): 957–966.

114. Tabibi, M., & Emadi, M. 2003. Variable cementation factor determination (empirical methods). Presented at the Middle East Oil Show, Bahrain, June 9–12, 2003. SPE-81485-MS. https://doi.org/10.2118/81485-MS.

115. Tinni, A. 2015. Pore connectivity and hydrocarbon storage in shale reservoirs. Ph.D. Dissertation, University of Oklahoma, Norman, Oklahoma.

116. Todd, H. B., & Evans, J. G. 2016. Improved oil recovery IOR pilot projects in the Bakken formation. Presented at the SPE Low Perm Symposium, Denver, Colorado, USA, May 5–6, 2016. SPE-180270-MS. https://doi.org/10.2118/180270-MS.

117. Ullman, W. J., & Aller, R. C. 1982. Diffusion coefficients in nearshore marine sediments1. *Limnology and Oceanography*, **27** (3): 552–556. https://doi.org/10.4319/lo.1982.27.3.0552.

118. US DOE, D. 2013. *EIA/ARI World Shale Gas and Shale Oil Resource Assessment* [EIA Report].

119. van Brakel, J., & Heertjes, P. M. 1974. Analysis of diffusion in macroporous media in terms of a porosity, a tortuosity and a constrictivity factor. *International Journal of Heat and Mass Transfer*, **17** (9): 1093–1103. https://doi.org/10.1016/0017-9310(74)90190-2.

120. Weissberg, H. L. 1963. Effective diffusion coefficient in porous media. *Journal of Applied Physics*, **34** (9): 2636–2639.

121. Winsauer, W. O., Shearin, H., Masson, P., & Williams, M. 1952. Resistivity of brine-saturated sands in relation to pore geometry. *AAPG Bulletin*, **36** (2): 253–277.

122. Worthington, P. 1998. Conjunctive interpretation of core and log data through association of the effective and total porosity models. *Geological Society, London, Special Publications*, **136** (1): 213–223.

123. Wyllie, M. R. J., & Rose, W. D. 1950. Some theoretical considerations related to the quantitative evaluation of the physical characteristics of reservoir rock from electrical log data. *Journal of Petroleum Technology*, **2** (04): 105–118. SPE-950105-G. https://doi.org/10.2118/950105-G.

124. Zhang, X., & Knackstedt, M. A. 1995. Direct simulation of electrical and hydraulic tortuosity in porous solids. *Geophysical Research Letters*, **22** (17): 2333–2336.

125. Zhang, Y., Ghanbarnezhad Moghanloo, R., & Davudov, D. 2019. Pore structure characterization of a shale sample using SEM images. Paper presented at the SPE Western Regional Meeting, San Jose, California, USA, April 2019. SPE-195352-MS. https://doi.org/10.2118/195352-MS.

126. Zhao, J., Hu, Q., Liu, K., Jin, Z., Dultz, S., Kaufmann, J., & Fan, Y. 2020. Pore connectivity characterization of shale using integrated wood's metal impregnation, microscopy, tomography, tracer mapping and porosimetry. *Fuel*, ***259****:* 116248. https://doi.org/10.1016/j.fuel.2019.116248.

127. Zheng, C., & Bennett, G. D. 2002. *Applied contaminant transport modeling* (Vol. 2). Wiley-Interscience New York.

128. Zou, C., Jin, X., Zhu, R., Gong, G., Sun, L., Dai, J., Meng, D., Wang, X., Li, J., Wu, S., Liu, X., Wu, J., & Jiang, L. 2015. Do Shale Pore Throats Have a Threshold Diameter for Oil Storage? *Scientific Reports*, **5** (1): 13619. https://doi.org/10.1038/srep13619.